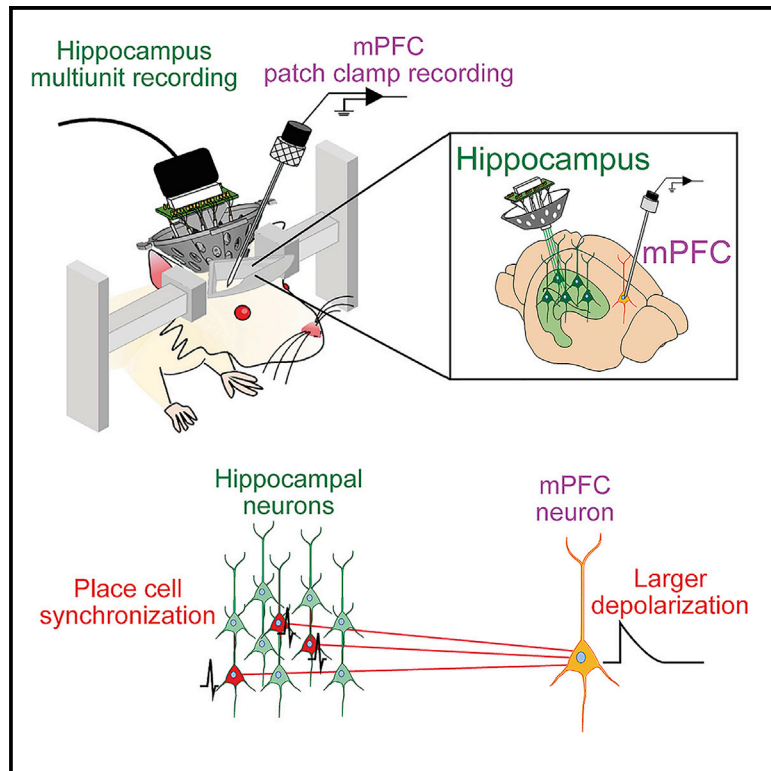


Prefrontal synaptic activation during hippocampal memory reactivation

Graphical abstract



Authors

Yuya Nishimura, Yuji Ikegaya,
Takuya Sasaki

Correspondence

tsasaki@mol.f.u-tokyo.ac.jp

In brief

Nishimura et al. find that medial prefrontal neurons receive depolarizing synaptic potentials when hippocampal place cells show synchronized spikes. This study provides direct physiological evidence of functional synaptic transmission from memory-encoding hippocampal neurons to prefrontal neurons.

Highlights

- Simultaneous multiunit recordings and whole-cell recordings are performed
- Prefrontal neurons depolarize during hippocampal place cell synchronization
- Hippocampal-prefrontal associations depend on memory-related spike patterns



Article

Prefrontal synaptic activation during hippocampal memory reactivation

Yuya Nishimura,¹ Yuji Ikegaya,^{1,2,3} and Takuya Sasaki^{1,4,5,*}¹Graduate School of Pharmaceutical Sciences, The University of Tokyo, 7-3-1 Hongo, Bunkyo-ku, Tokyo 113-0033, Japan²Center for Information and Neural Networks, National Institute of Information and Communications Technology, 1-4 Yamadaoka, Suita City, Osaka 565-0871, Japan³Institute for AI and Beyond, The University of Tokyo, Tokyo 113-0033, Japan⁴Precursory Research for Embryonic Science and Technology (PRESTO), Japan Science and Technology Agency (JST), 4-1-8 Honcho, Kawaguchi, Saitama 332-0012, Japan⁵Lead contact*Correspondence: tsasaki@mol.f.u-tokyo.ac.jp<https://doi.org/10.1016/j.celrep.2021.108885>

SUMMARY

Cooperative reactivation of hippocampal and prefrontal neurons is considered crucial for mnemonic processes. To directly record synaptic substances supporting the interregional interactions, we develop concurrent spike recordings of hippocampal neuronal ensembles and whole-cell patch-clamp recordings of medial prefrontal neurons in awake rats. We find that medial prefrontal neurons depolarize when hippocampal neurons synchronize. The depolarization in medial prefrontal neurons is larger when hippocampal place cells that encoded overlapping place fields and place cells that encoded a novel environment are synchronously reactivated. Our results suggest a functional circuit-synapse association that enables prefrontal neurons to read out specific memory traces from the hippocampus.

INTRODUCTION

A functional information transfer from the hippocampus (HPC) to the prefrontal cortex (PFC), via direct and indirect synaptic projections (Cenquizca and Swanson, 2007; Hoover and Vertes, 2007; Spellman et al., 2015), is pivotal to declarative memories (Eichenbaum, 2017; Tang and Jadhav, 2019). A possible neurophysiological substrate for the HPC-PFC communication is the reactivation of HPC neuronal ensembles that encoded previously experienced behavioral trajectories (Joo and Frank, 2018; Lee and Wilson, 2002; Wilson and McNaughton, 1994), typically associated with sharp-wave ripples (SWRs), a high-frequency oscillation event (150–250 Hz) in local field potential (LFP) signals (Buzsáki, 2015). The roles of HPC synchronized activity in memory functions are supported by the observations that memory-related behavioral performance is improved by optogenetic prolongation of awake HPC SWRs (Fernández-Ruiz et al., 2019) and impaired by selective disruption of awake (Gridchyn et al., 2020; Igata et al., 2021; Jadhav et al., 2012) and sleep (Girardeau et al., 2009) HPC SWRs. For widespread cortical regions outside the HPC, the strong excitation gain during HPC SWRs is suited to drive pronounced changes in ongoing neuronal activity, possibly serving as a substrate for inter-regional information transfer (Logothetis et al., 2012; Vaz et al., 2019). Several studies have shown that HPC SWRs can trigger coordinated reactivation of HPC-PFC cell ensembles that encode behaviorally relevant information (Benchenane et al., 2010; Jadhav et al., 2016; Peyrache et al., 2009; Shin et al., 2019), while a recent study

questioned this view by demonstrating that replay of animals' behavioral trajectories occurs almost independently between the HPC and the PFC (Kaefer et al., 2020), suggesting that this inter-regional information transfer is more complex than previously thought. While the precise HPC-PFC neuronal coordination is still under debate, it has been demonstrated at behavioral levels that reinforcing the HPC-PFC coordination during post-task periods facilitates memory consolidation (Maingret et al., 2016), which is suggestive of their potential roles in the redistribution of HPC labile mnemonic information into PFC long-term memory (Frankland and Bontempi, 2005; Tonegawa et al., 2018). For PFC neurons to efficiently read out information contents arising from the HPC, synchronized HPC cell ensemble patterns need to be properly transformed into synaptic inputs onto PFC neurons. The selective depolarization in a subset of PFC neurons then determines whether they participate in HPC-PFC coordinated activity. However, such neuronal inputs at a subthreshold level have not been directly measured, primarily owing to a lack of methodologies. To address this question, we simultaneously measured spike patterns of a HPC cell ensemble and a membrane potential of a medial PFC (mPFC) neuron from an awake rat by an integrated technique. While the ventral and intermediate HPC have been reported to more strongly project to the mPFC (Cenquizca and Swanson, 2007; Hoover and Vertes, 2007; Jay and Witter, 1991; Spellman et al., 2015) compared with the dorsal HPC, we recorded dorsal HPC neurons due to a technical limitation of recordings of sufficient numbers of HPC neuronal ensembles from the ventral and



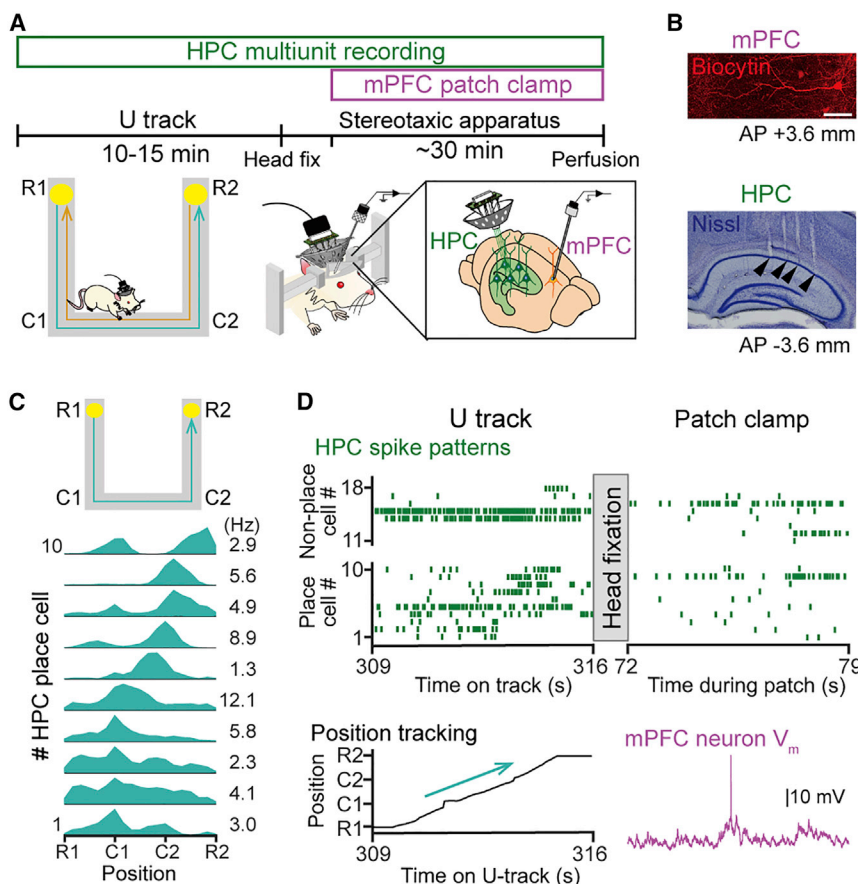


Figure 1. Simultaneous recordings of HPC neuronal spike patterns and mPFC neuronal membrane potential

(A) The experimental timeline. After spike patterns of HPC neurons were recorded from a freely moving rat in a U-track task, the rat was fixed on a stereotaxic apparatus, and a mPFC neuron was whole-cell recorded during a quiet awake period while the spike patterns of the identical hippocampal neurons were continuously recorded. Noteworthy locations are labeled R1, R2, C1, and C2. The cyan and orange arrows show trajectory patterns from R1 to R2 and from R2 to R1, respectively.

(B) Representative images of a biocytin-labeled mPFC neuron (top, scale bar = 50 μ m.) and a cresyl violet-stained brain section showing tetrode locations in the HPC (bottom, black arrowheads).

(C) (Top) An overview of the U-track with reward locations (yellow circles). The blue arrow shows a trajectory pattern from R1 to R2. (Bottom) Averaged firing-rate distributions of HPC place cells plotted as a function of positions linearized on the U-track. Place cells were arranged vertically in order of the positions of their place-field peaks.

(D) (Left) From top to bottom, a raster plot in which each row represents each HPC neuron, and each dot represents each spike, and instantaneous animals' positions during running from R1 to R2 on the U-track. In the raster plot, the 10 place cells were arranged as in (C), followed by eight non-place cells. (Right) Same as the left panel, but the bottom panel shows a membrane potential change in a PFC neuron during head fixation. See also [Figures S1–S3](#).

intermediate HPC. Thus, our results of the dorsal HPC-PFC interactions could be explained by indirect polysynaptic pathways through several brain areas such as the ventral HPC, thalamus, and neocortex.

RESULTS

Concurrent HPC multiunit recordings and mPFC whole-cell recordings

Rats were implanted with eight tetrodes directed at the HPC with a craniotomy over the mPFC for subsequent patch-clamp recordings ([Figure S1A](#)). During 2-to-3-week-post-surgery periods in which the tetrodes were lowered to the dorsal HPC pyramidal cell layer, the rats were trained to continuously run on a U-track to obtain a chocolate milk reward at both ends of the track and habituated to head restraint for subsequent patch-clamp recordings ([Figure 1A](#)). On a recording day, spike patterns were recorded from HPC putative pyramidal neurons in a 10-to-15-min familiar U-track task ([Figure 1B](#)). The well-trained rats completed 30.0 ± 2.5 running laps during a 10-min task period ($n = 16$ rats). A total of 135 HPC neurons were recorded. The majority of neurons were recorded from the CA1 area, whereas the minority of neurons were recorded from the CA2 area ([Figure S2A](#)). Of 84 place cells identified, 37 (44.1%) and 47 (55.9%) cells had unidirectional place fields depending on

running direction and bidirectional place fields independent of running directions, respectively ([Figures 1C](#) and [S3A–S3D](#)). The rats were then head-fixed under awake conditions, and whole-cell recordings were obtained from electrophysiologically and morphologically identified pyramidal neurons in layers 2–5 of the mPFC ($n = 18$ cells from 16 rats; [Figures 1B](#), [S2B](#), and [S2E](#)). Minimizing physical damage from surgical procedures and restricting time periods of all these experimental procedures within 2 h enabled continuous tracking of spikes of identical HPC cells ([Figures 1D](#) and [S2C](#)). In the post-task head-fixed periods, mPFC LFP signals did not contain apparent slow, delta, and spindle oscillations ([Figures S1C](#) and [S1D](#)) ([Maingret et al., 2016](#); [Peyrache et al., 2009](#); [Siapas and Wilson, 1998](#); [Sirota et al., 2003](#)), demonstrating that the rats were in awake quiescent states but not sleep states.

Synchronized reactivation of HPC neurons and mPFC membrane potentials

During whole-cell recordings from mPFC neurons, HPC neurons were synchronously reactivated ([Figures 2A](#) and [S3E–S3G](#)), consistent with previous studies ([Eschenko et al., 2008](#); [Kudrimoti et al., 1999](#); [Norimoto et al., 2018](#)). Based on the length of SWR-associated sequential replays reported previously ([Buzsáki, 2015](#); [Carr et al., 2011](#)) and sufficient sample numbers of synchronous events in our datasets ([Figures S3E–S3G](#) and

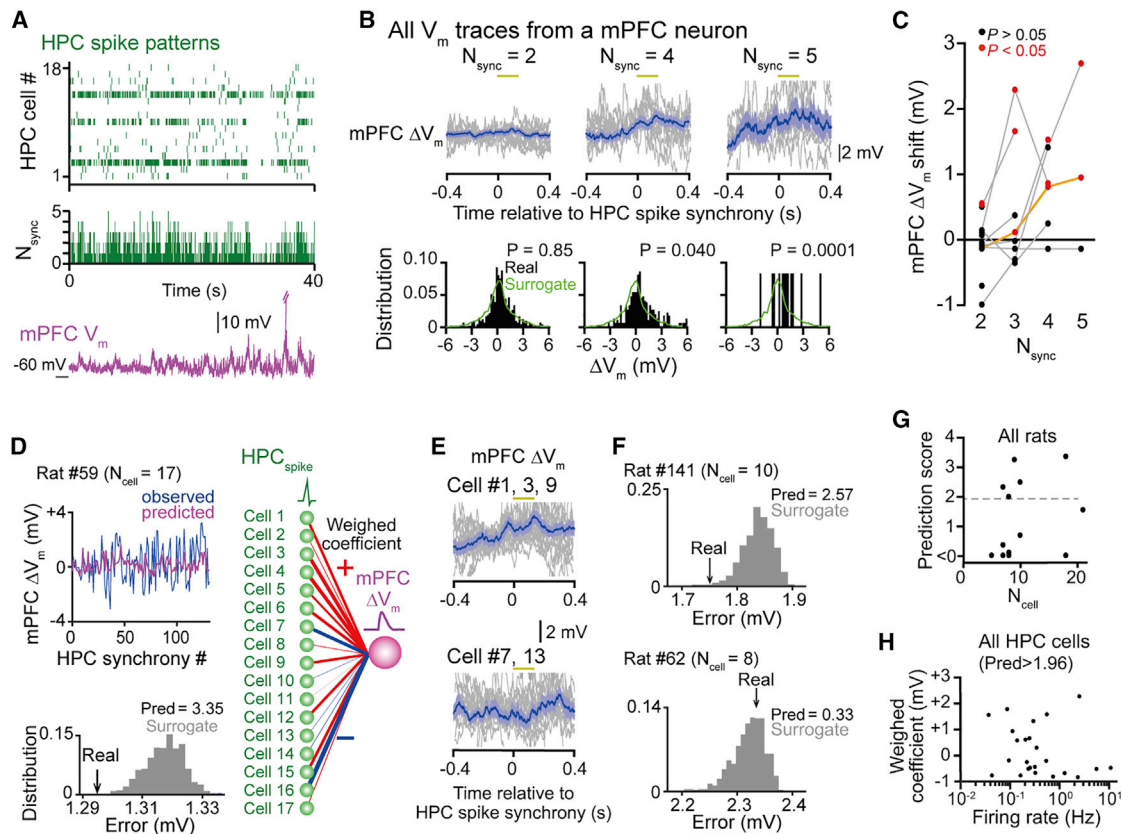


Figure 2. Prediction of a mPFC neuronal membrane potential from synchronized spikes of HPC neurons

(A) Simultaneous recordings of spike patterns of HPC neurons (top), the numbers of co-active HPC neurons (middle), and subthreshold V_m in a mPFC neuron (bottom). Spikes were truncated for better visualization.

(B) (Top) Membrane potential traces of a representative mPFC neuron aligned to the time of synchronous firing of two ($N_{sync} = 2$), four ($N_{sync} = 4$), and five ($N_{sync} = 5$) HPC neurons. Individual traces are shown by thin gray lines, and the averages and SEM are shown by thick blue lines and thin blue regions, respectively. (Bottom) Distribution of membrane potential changes in the mPFC neuron at individual HPC synchronized events. The real distributions were compared with those in the corresponding surrogates in which the time of HPC synchrony was randomly shuffled (green lines).

(C) Shifts in average mPFC ΔV_m against the number of synchronized HPC neurons ($n = 13$ mPFC neurons from 13 rats with >4 HPC cells). Each line represents a recording from a mPFC neuron. The example mPFC neuron shown in (B) is highlighted by the orange line. For each plot at each N_{sync} and at each mPFC, a p value was independently computed by a comparison between real and surrogate distributions by the Kolmogorov-Smirnov test. Red dots show statistically significant results.

(D) (Top) For a representative mPFC neuron from a rat (rat #59), a linear regression analysis was applied to predict mPFC ΔV_m at the time of each HPC synchrony from synchronized spike patterns of HPC cells (blue, observed; magenta, predicted). (Bottom) An error of prediction from the real data (black arrow) was compared with errors (in mV) of prediction from surrogate datasets in which observed ΔV_m were randomly shuffled across HPC synchrony (gray distribution). A prediction score was computed as a negative value of a Z score defined by the surrogate distribution. (Right) Distribution of weight for each cell used for the prediction. Red and blue edges represent positive and negative relationships with mPFC ΔV_m , respectively.

(E) Membrane potential traces of the mPFC neuron aligned to the time of synchronous spikes of HPC neurons indicated. Individual traces are shown by thin gray lines, and the averages and SEM are shown by thick blue lines and thin blue regions, respectively.

(F) As in the bottom panel of (D), but for the other two mPFC neurons from two rats.

(G) Prediction scores of all 13 mPFC neurons (from 13 rats) plotted against the number of HPC neurons. Significantly predicted fractions with $p < 0.05$ defined by prediction scores are shown above the dotted line.

(H) Distribution of weight values of individual HPC neurons plotted against their firing rates in rats with significant prediction scores ($n = 43$ HPC cells from 5 rats). $R = -0.072$, $p = 0.60$.

See also Figure S4.

S4J), we here used a time window of 100 ms to define HPC synchronization events. We assessed whether these HPC synchronization events impacted subthreshold potentials of mPFC neurons. For each mPFC neuron, distributions of mPFC membrane potential changes (ΔV_m) were analyzed for different numbers of HPC synchronized cells (N_{sync}), ranging from 2 to 5

cells (an example mPFC neuron is shown in Figure 2B). Assuming that the majority of HPC reactivation ranges within 100 ms and leads over mPFC activity by tens of milliseconds (Peyrache et al., 2009; Place et al., 2016), mPFC ΔV_m was computed from a post-event 0-to-150-ms time window after the onset of HPC synchronization. Here, HPC synchronization

events that occurred within 200 ms from prior HPC SWRs were excluded from our analysis, as they potentially represented the second and subsequent events involved in ripple bursts (Yamamoto and Tonegawa, 2017). In the example mPFC neuron in Figure 2B, mPFC ΔV_m distributions for N_{sync} of 3–5, but not for 2, showed significant rightward (depolarizing) shifts, compared with surrogate distributions in which each mPFC ΔV_m was randomly extracted from the same mPFC membrane voltage trace, demonstrating that larger mPFC depolarization occurred significantly more often than by chance. Results from all mPFC neurons are summarized in Figure 2C ($n = 13$ mPFC neurons from 13 rats with >4 HPC neurons), in which each line represents each mPFC neuron, and each red dot indicates the average of a distribution with a significant ($p < 0.05$) rightward shift, defined by a comparison between real and surrogate distributions by the Kolmogorov-Smirnov test. While mPFC ΔV_m distributions at two HPC cell synchronizations ($N_{\text{sync}} = 2$) were indistinguishable from chance level in the majority (84.6%) of datasets ($n = 13$ mPFC neurons), the significant effects tended to be more prominent as the number of synchronized HPC cells increased (Figure 2C; 37.5% [3/8], 50.0% [3/6], and 66.6% [2/3] for $N_{\text{sync}} = 3, 4, \text{ and } 5$, respectively; no multiple comparisons were applied). These significant results were also observed when statistical tests were performed for comparisons between the distributions of mPFC ΔV_m in a post-event 0-to-150-ms window and those of the corresponding baseline mPFC ΔV_m (Figure S4H). While connectivity patterns with the HPC differ between the prefrontal (PL) subregion and anterior cingulate cortex (ACC) (Heidbreder and Groenewegen, 2003; Jay and Witter, 1991), these significant effects were observed in both regions (Figure S4N). Consistently, several mPFC cells showed similar significant depolarizing shifts during HPC SWRs ($n = 6$ out of 17 cells from 15 rats with HPC SWRs; Figures S4D and S4E). The same analysis was performed with a pre-event 0-to-150-ms window assuming that mPFC neuronal activity precedes HPC synchronization events (Figure S4F) and a post-event 350-to-500-ms window assuming that HPC synchronization events influence mPFC neuronal activity at more remote time (Figure S4G). In these cases, the significant fractions of mPFC ΔV_m distributions were prominently lowered (13.3% and 6.7%, respectively), confirming that HPC synchronization events preceded significant mPFC membrane potential changes. We thus chose the post-event 0-to-150-ms window in the following analyses.

The datasets shown in Figure 2C demonstrate that several mPFC neurons exhibited significant ΔV_m distribution shifts in response to synchronization with relatively low numbers of synchronous HPC cells (e.g., $N_{\text{sync}} = 3$), whereas the other mPFC neurons exhibited no significant shifts even at larger numbers of synchronous HPC cells (e.g., $N_{\text{sync}} = 4$ –5). To further examine whether these differences may be due to different numbers of samples or the variability of samples used to compute Figure 2C, we classified mPFC neurons into two types: (1) significant mPFC cells that had at least one significant plot for N_{sync} from 2 to 5 ($n = 7$ cells, shown in red lines in Figure S4I) and (2) non-significant mPFC cells that had no significant plots for all N_{sync} ($n = 6$ cells, shown in blue lines in Figure S4I). Between the two cell groups, no significant differences were found in the numbers of HPC synchronous events and the variance of mPFC ΔV_m distributions for

all N_{sync} (Figure S4J; $p > 0.05$, Tukey's test). These results confirm that differences in the sensitivity to HPC cell synchronization across mPFC neurons are not simply explained by differences in the numbers and the variability of samples.

We next examined whether individual HPC synchronized spike patterns were associated with mPFC ΔV_m using a linear regression analysis with a leave-one-out cross-validation (Figure 2D). HPC synchronization events with at least three spiking HPC cells were used as a predictor vector s to predict the corresponding mPFC ΔV_m . For each mPFC neuron, a prediction error (in mV) was computed as an average of differences between observed and predicted mPFC ΔV_m over all events. To assess the significance of predictability, a prediction score was defined as a negative value of the Z score computed from 1,000 surrogate datasets in which the order of mPFC ΔV_m , target variables, was randomly shuffled across all HPC synchronization events (an example mPFC neuron is shown in Figure 2D, and an additional two mPFC neurons are shown in Figure 2F). Of 13 mPFC neurons from 13 rats (with >4 HPC cells), 5 mPFC neurons (from 5 rats) had a significantly positive prediction score >1.96 ($p < 0.05$), while the predictability was not apparently related to the number of recorded HPC cells (Figure 2G). Neurons with significantly positive scores were observed in both the PL and ACC (Figure S4O). The same results were observed when surrogate datasets were created by shuffling the order of HPC spikes across synchronization events and maintaining the total number of spikes within each cell (Figure S4L) or by shuffling the order of HPC synchronization events and maintaining the total numbers of HPC events at individual N_{sync} (Figure S4M). In predictable datasets, 60.5% of HPC neurons had positive weighed coefficients (Figure 2H, $n = 43$ HPC cells from 5 rats), implying that these HPC neurons have depolarizing, rather than hyperpolarizing, effects on mPFC neuronal membrane potentials. No significant correlations were found between weighed coefficients and baseline firing rates of individual HPC neurons ($R = -0.078$, $p = 0.57$). Taken together, these results demonstrate that membrane potential changes in some mPFC cells are predictable from the summation of weighed synchronized spike patterns of HPC cells. With the time windows of 0–150 ms before and 350–500 ms after HPC synchronization, mPFC ΔV_m was not predictive (Figures S4F and S4G), again confirming the HPC-leading-mPFC directionality.

Reactivation of HPC place cells induces mPFC depolarization

The findings of the HPC-mPFC ΔV_m relationship next led us to ask whether HPC cells encoding behaviorally relevant information more strongly affect mPFC ΔV_m in subsequent quiescent periods. Distributions of mPFC ΔV_m were constructed for different numbers of synchronized HPC place cells (Figure 3A). Overall, mPFC ΔV_m was larger at the occurrence of HPC synchronization events with place cell spikes, compared to that without place cell spikes (Figure 3B; 0 versus 1, $Z = 3.84$, $p = 3.6 \times 10^{-4}$; 0 versus ≥ 2 , $Z = 3.22$, $p = 0.0039$; Mann-Whitney U test followed by Bonferroni correction; $p = 9.5 \times 10^{-5}$, Kruskal-Wallis test). No differences in mPFC ΔV_m were found between HPC synchronization events with one place cell and with two or more place cells (1 versus ≥ 2 , $Z = 0.18$, $p > 0.99$).

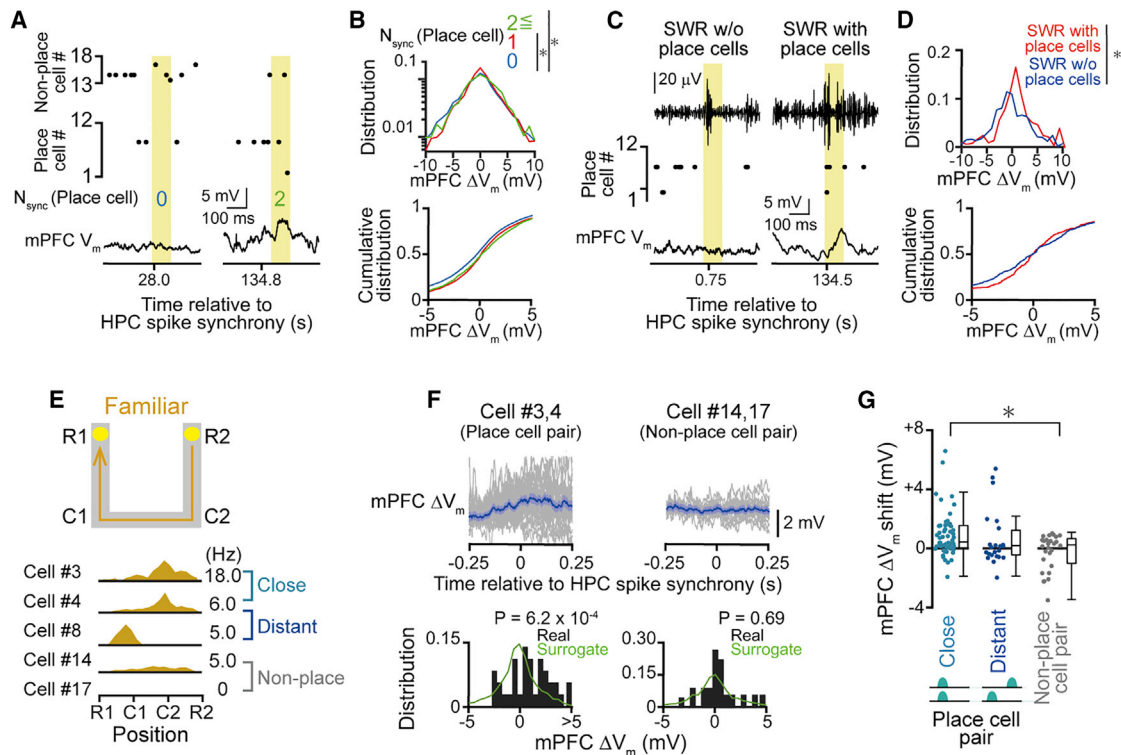


Figure 3. Larger depolarization in mPFC neurons during synchronous spikes of HPC place cells

(A) Representative synchronized spikes including zero (left, $N_{\text{sync}}[\text{place cell}] = 0$) and two (right, $N_{\text{sync}}[\text{place cell}] = 2$) HPC place cells (top) and the corresponding membrane potential changes in a mPFC neuron (bottom). Yellow regions represent 0–100 ms after the onset of HPC synchronization.

(B) (Top) Distributions of membrane potential changes in all mPFC neurons individually plotted for different numbers (zero, one, and two or more) of synchronized HPC place cells ($n = 5,704, 4,602$, and $2,507$ events, respectively). * $p < 0.05$, Mann-Whitney U test followed by Bonferroni correction. (Bottom) The same data are plotted as cumulative distributions.

(C) HPC SWRs without (left) and with (right) HPC place cell spikes (top) and the corresponding membrane potential changes in a mPFC neuron (bottom).

(D) As in (B) but plotted against HPC SWRs without and with place cell spikes ($n = 660$ and 747 SWRs, respectively). * $p < 0.05$, Mann-Whitney U test.

(E) Schematic illustration of the U-track for well-trained rats (top) and averaged firing-rate distributions of representative HPC place cells on the U-track (bottom).

(F) Membrane potential changes in the mPFC neuron aligned to the time of synchronous spikes of a HPC place cell pair (left) or non-place cell pair (right).

(G) Average membrane potential changes in mPFC neurons at the time of synchronized spikes of place cell pairs with their place fields at close and distant locations and nonspatial cell pairs ($n = 57, 23$, and 27 HPC cell pairs, respectively). Each dot represents each place cell pair, and the corresponding boxplots are shown beside the dots. * $p < 0.05$, Mann-Whitney U test followed by Bonferroni correction.

In addition, we tested the effects of HPC SWRs that contained or did not contain place cell spikes on mPFC ΔV_m . The frequencies of HPC SWRs with and without place cells were 0.19 ± 0.05 Hz and 0.12 ± 0.03 Hz, respectively ($n = 13$ rats). Overall mPFC ΔV_m during HPC SWRs with place cell spikes was significantly larger than that without place cell spikes (Figures 3C and 3D; $Z = 2.28$, $p = 0.023$, Mann-Whitney U test). We next directly analyzed whether synchronous events including specific place cell pairs more strongly affected mPFC ΔV_m (Figures 3E and 3F). Computing the distributions of mPFC ΔV_m from all possible HPC cell pairs (showing more than four synchronized spikes during a patch-clamp recording period) revealed that synchronization of place cell pairs showed significantly larger depolarization shifts of mPFC ΔV_m than that of non-place cell pairs (Figure 3G; $n = 80$ and 27 cell pairs, $Z = 2.13$, $p = 0.033$, Mann-Whitney U test). Moreover, there was a significantly larger depolarization of mPFC ΔV_m at synchronization of place cell pairs with their inter-field distance < 30 cm (close pair, $n = 57$ cell pairs), but not at

the distance > 60 cm (distant pair, $n = 23$ cell pairs), than that of non-place cell pairs (Figure 3G; close versus non-place, $Z = 2.66$, $p = 0.016$; distant versus non-place, $Z = 0.35$, $p > 0.99$, Mann-Whitney U test followed by Bonferroni correction; $p = 0.017$, Kruskal-Wallis test). These significant effects were not observed when time windows to detect HPC synchronization events were shortened to 50 ms or shorter. These results suggest that reactivation of HPC place cells with overlapping spatial representations (Kudrimoti et al., 1999; Lee and Wilson, 2002; O'Neill et al., 2008; Wilson and McNaughton, 1994) exerts stronger synaptic influences on downstream mPFC neurons than those with nonoverlapping representations.

Reactivation of HPC place cells in a novel environment induces mPFC depolarization

During rest/sleep periods, especially after novel learning, the HPC-PFC circuits exhibit enhanced coordination of neuronal co-firing (O'Neill et al., 2008; Peyrache et al., 2009; Tang

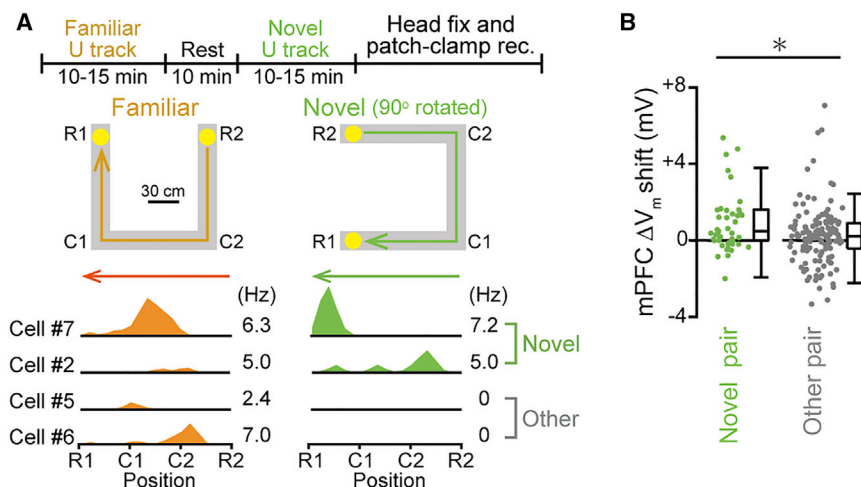


Figure 4. Larger depolarization in mPFC neurons during synchronous spikes of HPC place cells (novel)

(A) (Top to bottom) The timeline of experiments including the novel U-track task, schematic illustrations of the U-tracks, and spatial firing distributions of four typical HPC cells.

(B) As in Figure 3G but plotted for pairs of HPC place cells (novel) and the other neuron pairs ($n = 43$ and 145 HPC cell pairs, respectively). $*p < 0.05$, Mann-Whitney U test.

See also Figure S3.

et al., 2017). We next tested the effects of novel learning on HPC-mPFC interactions. After recording from the familiar task, the U-track was rotated counterclockwise by 90 degrees. The rats then performed a 10–15-min U-track task with this novel positioning, termed a novel U-track task (Figure 4A). The rats run well on the novel track, with 15.8 ± 3.6 running laps per 10 min ($n = 8$ rats). Out of 76 HPC cells from 8 rats tested, 42 (55.3%) cells exhibited spatial firing in the novel task, termed “place cells (novel)” (Figures 4A and S2H). In Figure 4B, membrane potential changes in mPFC neurons ($n = 8$ mPFC neurons from 8 rats) were computed at synchronization of pairs of HPC place cells (novel) ($n = 43$ cell pairs) or the other cell pairs ($n = 145$ cell pairs) that composed the non-place cells in the novel task (including place cells identified in the familiar task only). Overall, we found significantly larger depolarization when pairs of HPC place cells (novel) were synchronized (Figure 4B; $Z = 2.37$, $p = 0.018$, Mann-Whitney U test).

We further characterized place cells (novel) based on changes in spatial firing patterns across the two tasks. Out of the 42 HPC place cells (novel), 8 cells (19.0%) were place cells in the novel task only (classified as “appear” in Figure S2I), whereas the other 34 cells (81.0%) were classified as place cells in both the familiar and novel tasks. Of the 34 cells, 9 had place fields at the same locations across the two tasks (classified as “stable” in Figure S2I), whereas the other 25 cells changed the locations of at least one place field (classified as “remap” types in Figure S2I). Assuming that the 33 place cells (novel) classified as appear or remap types were novelty-responsive HPC cells that more specifically encoded the novel task conditions, compared with the other cells, the same analysis was applied to these cell populations. Similarly, we observed significantly larger depolarization when these novelty-responsive HPC cell pairs were synchronized ($n = 35$ and 153 cell pairs, $Z = 1.97$, $p = 0.048$, Mann-Whitney U test). These results suggest that newly acquired information is more effectively transferred from the HPC cell ensembles to mPFC neurons during post-learning time periods.

DISCUSSION

There is ample evidence that the HPC-PFC communications are involved in memory functions (Eichenbaum, 2017; Tang and Jadhav, 2019), possibly by transferring information of neuronal activity patterns from the HPC to the PFC circuit for stabilization of memory traces (Euston et al., 2007; Jadhav et al., 2016; Maingret et al., 2016; Peyrache et al., 2009). In addition to the accumulating evidence, our study with concurrent HPC multiunit recordings and mPFC whole-cell recordings revealed direct neurophysiological evidence of the substantial association of HPC synchronization events with mPFC subthreshold potentials (several millivolts in size). Considering the fact that even 1 mV depolarizing force was sufficient to produce postsynaptic neuronal spikes (Ikegaya et al., 2013), we find that the functional neurotransmission is a possible neurophysiological basis for the coordinated activation of spike trains across the HPC-PFC circuits (Benchenane et al., 2010; Jadhav et al., 2016; Peyrache et al., 2009; Shin et al., 2019). Interestingly, a subset of, but not all, mPFC neuronal membrane potentials were specifically responsive to synchronous HPC spike patterns (Figures 2C and 2G). These observations suggest that the sensitivity of mPFC neurons to HPC spike activity is heterogeneous, possibly due to differences in their anatomical and physiological properties, such as functional connectivity with the HPC and intrinsic excitability.

We note that our results showed a correlative, but not causal, relationship between HPC spike synchronization and mPFC membrane potentials. One possible scenario is that both the HPC and the mPFC activity might be induced by a common external drive from the other brain regions not measured in our study. Another point to note is that our results do not imply monosynaptic connections from the HPC to the mPFC. Considering the anatomical observations that dorsal HPC neurons send a minor projection to the mPFC (Cenquizca and Swanson, 2007; Jay and Witter, 1991), the HPC-mPFC link we observed at the subthreshold level is likely mediated by indirect polysynaptic routes through the intermediate and ventral HPC having strong direct projections to the mPFC (Cenquizca and Swanson, 2007; Hoover and Vertes, 2007; Spellman et al., 2015), the

nucleus reuniens of the thalamus, and the other neocortical areas (Ito et al., 2015). These issues will be addressed in future experiments with the multisite electrophysiological recordings from brain regions.

Tang et al. (2017) have demonstrated an arousal state-dependent modulation of mPFC neurons by HPC SWRs possibly due to the differences in neuromodulatory tone; excitation and inhibition of neuronal spikes occurred in almost equivalent proportions of mPFC neurons during awake SWRs (Jadhav et al., 2016), whereas excitatory modulation is more dominant in mPFC neurons during sleep SWRs (Siapas and Wilson, 1998). In our patch-clamp recording conditions, the head-fixed rats were in quiescent awake states. Considering our results that the HPC-PFC transmission was predominately depolarized, which possibly results in net increases in firing rates of mPFC neurons, the rats' arousal states in this study might be closer to the sleep states observed by Tang et al. (2017). Together with the observation that awake HPC-PFC reactivation more accurately encoded behavioral experiences than sleep reactivation (Tang et al., 2017), the HPC-mPFC interactions observed in our study might become more reliable and contain more inhibitory effects under active awake conditions.

The functional transmission in which behaviorally relevant information (e.g., similar spatial representations) encoded by HPC cell ensembles led to stronger depolarization in mPFC neurons might be necessary to generate coherent replay across the HPC-PFC circuits (Shin et al., 2019). Furthermore, the functional transmission in which novelty relevant information also led to stronger depolarization in mPFC neurons might implicate an efficient mechanism for mPFC neurons to preferentially respond to newly learned knowledge structures arising from the HPC (Shin et al., 2019; Tang et al., 2017). The learning-dependent synaptic influences might be useful to induce synaptic plasticity that would support long-term memory storage of new labile traces across the HPC-PFC circuits. Further studies are required to elucidate how mPFC neurons isolate information carried by specific novelty-related synapses from the other competing synaptic inputs. Given that timed spike sequences and neurotransmission are common neurophysiological mechanisms for all neurons in the brain, our findings are not just limited to the HPC-PFC circuits and could be extended to the other brain areas as a principle to achieve efficient information transfer across inter-regional neuronal ensembles.

STAR★METHODS

Detailed methods are provided in the online version of this paper and include the following:

- KEY RESOURCES TABLE
- RESOURCE AVAILABILITY
 - Lead contact
 - Materials availability
 - Data and code availability
- EXPERIMENTAL MODEL AND SUBJECT DETAILS
- METHOD DETAILS
 - Behavioral training on a U-shaped track
 - Surgical procedures

- Adjusting electrode depth
- Electrophysiological recording in U track tasks
- *In vivo* patch-clamp recordings
- Histological analysis to confirm tetrode locations and patch-clamped cells

● QUANTIFICATION AND STATISTICAL ANALYSIS

- Spike sorting of hippocampal neurons
- Spatial firing patterns of individual hippocampal neurons
- Detection of HPC synchronized spikes and SWRs
- Detection of neocortical oscillations
- Membrane potential changes in mPFC neurons during HPC synchronization
- Prediction of mPFC membrane potential changes from HPC synchronized spike patterns
- Statistics

SUPPLEMENTAL INFORMATION

Supplemental Information can be found online at <https://doi.org/10.1016/j.celrep.2021.108885>.

ACKNOWLEDGMENTS

This work was supported by KAKENHI (19H04897, 17H05939, and 20H03545) from the Japan Society for the Promotion of Science (JSPS), a Precursory Research for Embryonic Science and Technology grant (JPMJPR1785) from the Japan Science and Technology Agency (JST), and a grant from the Advanced Research & Development Programs for Medical Innovation (1041630) of the Japan Agency for Medical Research and Development (AMED) to T.S.; funds from the JST Exploratory Research for Advanced Technology (JPMJER1801) and the AMED Strategic International Brain Science Research Promotion Program (18dm0307007h0001) to Y.I.; and a JSPS Research Fellowship for Young Scientists to Y.N.

AUTHOR CONTRIBUTIONS

Y.N. and T.S. designed the study. Y.N. performed the surgery and acquired the electrophysiological data, and Y.N. and T.S. performed the analysis and prepared all figures. Y.I. supervised the project. T.S. wrote the main manuscript text, and all authors reviewed the main manuscript text.

DECLARATION OF INTERESTS

The authors declare no competing interests.

Received: September 29, 2020

Revised: December 7, 2020

Accepted: February 25, 2021

Published: March 23, 2021

REFERENCES

- Aoki, Y., Igata, H., Ikegaya, Y., and Sasaki, T. (2019). The Integration of Goal-Directed Signals onto Spatial Maps of Hippocampal Place Cells. *Cell Rep.* 27, 1516–1527.e1515.
- Benchenane, K., Peyrache, A., Khamassi, M., Tierney, P.L., Gioanni, Y., Battaglia, F.P., and Wiener, S.I. (2010). Coherent theta oscillations and reorganization of spike timing in the hippocampal- prefrontal network upon learning. *Neuron* 66, 921–936.
- Buzsáki, G. (2015). Hippocampal sharp wave-ripple: A cognitive biomarker for episodic memory and planning. *Hippocampus* 25, 1073–1188.

- Carr, M.F., Jadhav, S.P., and Frank, L.M. (2011). Hippocampal replay in the awake state: a potential substrate for memory consolidation and retrieval. *Nat. Neurosci.* *14*, 147–153.
- Cenquizca, L.A., and Swanson, L.W. (2007). Spatial organization of direct hippocampal field CA1 axonal projections to the rest of the cerebral cortex. *Brain Res. Brain Res. Rev.* *56*, 1–26.
- Csicsvari, J., Hirase, H., Czúrkó, A., Mamiya, A., and Buzsáki, G. (1999). Oscillatory coupling of hippocampal pyramidal cells and interneurons in the behaving rat. *J. Neurosci.* *19*, 274–287.
- Eichenbaum, H. (2017). Prefrontal-hippocampal interactions in episodic memory. *Nat. Rev. Neurosci.* *18*, 547–558.
- Eschenko, O., Ramadan, W., Mölle, M., Born, J., and Sara, S.J. (2008). Sustained increase in hippocampal sharp-wave ripple activity during slow-wave sleep after learning. *Learn. Mem.* *15*, 222–228.
- Euston, D.R., Tatsuno, M., and McNaughton, B.L. (2007). Fast-forward playback of recent memory sequences in prefrontal cortex during sleep. *Science* *318*, 1147–1150.
- Fernández-Ruiz, A., Oliva, A., Fermino de Oliveira, E., Rocha-Almeida, F., Tingley, D., and Buzsáki, G. (2019). Long-duration hippocampal sharp wave ripples improve memory. *Science* *364*, 1082–1086.
- Frankland, P.W., and Bontempi, B. (2005). The organization of recent and remote memories. *Nat. Rev. Neurosci.* *6*, 119–130.
- Girardeau, G., Benchenane, K., Wiener, S.I., Buzsáki, G., and Zugaro, M.B. (2009). Selective suppression of hippocampal ripples impairs spatial memory. *Nat. Neurosci.* *12*, 1222–1223.
- Gridchyn, I., Schoenenberger, P., O'Neill, J., and Csicsvari, J. (2020). Assembly-Specific Disruption of Hippocampal Replay Leads to Selective Memory Deficit. *Neuron* *106*, 291–300.e6.
- Harris, K.D., Henze, D.A., Csicsvari, J., Hirase, H., and Buzsáki, G. (2000). Accuracy of tetrode spike separation as determined by simultaneous intracellular and extracellular measurements. *J. Neurophysiol.* *84*, 401–414.
- Heidbreder, C.A., and Groenewegen, H.J. (2003). The medial prefrontal cortex in the rat: evidence for a dorso-ventral distinction based upon functional and anatomical characteristics. *Neurosci. Biobehav. Rev.* *27*, 555–579.
- Hoover, W.B., and Vertes, R.P. (2007). Anatomical analysis of afferent projections to the medial prefrontal cortex in the rat. *Brain Struct. Funct.* *212*, 149–179.
- Igata, H., Ikegaya, Y., and Sasaki, T. (2021). Prioritized experience replays on a hippocampal predictive map for learning. *Proc. Natl. Acad. Sci. USA* *118*, e2011266118.
- Ikegaya, Y., Sasaki, T., Ishikawa, D., Honma, N., Tao, K., Takahashi, N., Minamisawa, G., Ujita, S., and Matsuki, N. (2013). Interpyramid spike transmission stabilizes the sparseness of recurrent network activity. *Cereb. Cortex* *23*, 293–304.
- Ito, H.T., Zhang, S.J., Witter, M.P., Moser, E.I., and Moser, M.B. (2015). A prefrontal-thalamo-hippocampal circuit for goal-directed spatial navigation. *Nature* *522*, 50–55.
- Jadhav, S.P., Kemere, C., German, P.W., and Frank, L.M. (2012). Awake hippocampal sharp-wave ripples support spatial memory. *Science* *336*, 1454–1458.
- Jadhav, S.P., Rothschild, G., Roumis, D.K., and Frank, L.M. (2016). Coordinated Excitation and Inhibition of Prefrontal Ensembles during Awake Hippocampal Sharp-Wave Ripple Events. *Neuron* *90*, 113–127.
- Jay, T.M., and Witter, M.P. (1991). Distribution of hippocampal CA1 and subicular efferents in the prefrontal cortex of the rat studied by means of anterograde transport of Phaseolus vulgaris-leucoagglutinin. *J. Comp. Neurol.* *313*, 574–586.
- Jog, M.S., Connolly, C.I., Kubota, Y., Iyengar, D.R., Garrido, L., Harlan, R., and Graybiel, A.M. (2002). Tetrode technology: advances in implantable hardware, neuroimaging, and data analysis techniques. *J. Neurosci. Methods* *117*, 141–152.
- Joo, H.R., and Frank, L.M. (2018). The hippocampal sharp wave-ripple in memory retrieval for immediate use and consolidation. *Nat. Rev. Neurosci.* *19*, 744–757.
- Kaefer, K., Nardin, M., Blahna, K., and Csicsvari, J. (2020). Replay of Behavioral Sequences in the Medial Prefrontal Cortex during Rule Switching. *Neuron* *106*, 154–165.e6.
- Kloosterman, F., Davidson, T.J., Gomperts, S.N., Layton, S.P., Hale, G., Nguyen, D.P., and Wilson, M.A. (2009). Micro-drive array for chronic in vivo recording: drive fabrication. *J. Vis. Exp.* (26), 1094.
- Kudrimoti, H.S., Barnes, C.A., and McNaughton, B.L. (1999). Reactivation of hippocampal cell assemblies: effects of behavioral state, experience, and EEG dynamics. *J. Neurosci.* *19*, 4090–4101.
- Latchoumane, C.V., Ngo, H.V., Born, J., and Shin, H.S. (2017). Thalamic Spindles Promote Memory Formation during Sleep through Triple Phase-Locking of Cortical, Thalamic, and Hippocampal Rhythms. *Neuron* *95*, 424–435.e6.
- Lee, D., and Lee, A.K. (2017). In Vivo Patch-Clamp Recording in Awake Head-Fixed Rodents. *Cold Spring Harb. Protoc.* *2017*, pdb.prot095802.
- Lee, A.K., and Wilson, M.A. (2002). Memory of sequential experience in the hippocampus during slow wave sleep. *Neuron* *36*, 1183–1194.
- Logothetis, N.K., Eschenko, O., Murayama, Y., Augath, M., Stuedel, T., Evrard, H.C., Besserve, M., and Oeltermann, A. (2012). Hippocampal-cortical interaction during periods of subcortical silence. *Nature* *491*, 547–553.
- Maingret, N., Girardeau, G., Todorova, R., Goutierre, M., and Zugaro, M. (2016). Hippocampo-cortical coupling mediates memory consolidation during sleep. *Nat. Neurosci.* *19*, 959–964.
- Narikiyo, K., Mizuguchi, R., Ajima, A., Shiozaki, M., Hamanaka, H., Johansen, J.P., Mori, K., and Yoshihara, Y. (2020). The claustrum coordinates cortical slow-wave activity. *Nat. Neurosci.* *23*, 741–753.
- Nguyen, D.P., Layton, S.P., Hale, G., Gomperts, S.N., Davidson, T.J., Kloosterman, F., and Wilson, M.A. (2009). Micro-drive array for chronic in vivo recording: tetrode assembly. *J. Vis. Exp.* (26), 1098.
- Norimoto, H., Makino, K., Gao, M., Shikano, Y., Okamoto, K., Ishikawa, T., Sasaki, T., Hioki, H., Fujisawa, S., and Ikegaya, Y. (2018). Hippocampal ripples down-regulate synapses. *Science* *359*, 1524–1527.
- O'Neill, J., Senior, T.J., Allen, K., Huxter, J.R., and Csicsvari, J. (2008). Reactivation of experience-dependent cell assembly patterns in the hippocampus. *Nat. Neurosci.* *11*, 209–215.
- Okada, S., Igata, H., Sasaki, T., and Ikegaya, Y. (2017). Spatial Representation of Hippocampal Place Cells in a T-Maze with an Aversive Stimulation. *Front. Neural Circuits* *11*, 101.
- Peyrache, A., Khamassi, M., Benchenane, K., Wiener, S.I., and Battaglia, F.P. (2009). Replay of rule-learning related neural patterns in the prefrontal cortex during sleep. *Nat. Neurosci.* *12*, 919–926.
- Place, R., Farovik, A., Brockmann, M., and Eichenbaum, H. (2016). Bidirectional prefrontal-hippocampal interactions support context-guided memory. *Nat. Neurosci.* *19*, 992–994.
- Redish, A.D. (2009). *MClust 3.5, Free-Ware Spike Sorting (University of Minnesota)*. <http://redishlab.neuroscience.umn.edu/MClust/MClust.html>.
- Schmitzer-Torbert, N., Jackson, J., Henze, D., Harris, K., and Redish, A.D. (2005). Quantitative measures of cluster quality for use in extracellular recordings. *Neuroscience* *131*, 1–11.
- Shin, J.D., Tang, W., and Jadhav, S.P. (2019). Dynamics of Awake Hippocampal-Prefrontal Replay for Spatial Learning and Memory-Guided Decision Making. *Neuron* *104*, 1110–1125.e7.
- Siapas, A.G., and Wilson, M.A. (1998). Coordinated interactions between hippocampal ripples and cortical spindles during slow-wave sleep. *Neuron* *21*, 1123–1128.
- Sirota, A., Csicsvari, J., Buhl, D., and Buzsáki, G. (2003). Communication between neocortex and hippocampus during sleep in rodents. *Proc. Natl. Acad. Sci. USA* *100*, 2065–2069.

- Spellman, T., Rigotti, M., Ahmari, S.E., Fusi, S., Gogos, J.A., and Gordon, J.A. (2015). Hippocampal-prefrontal input supports spatial encoding in working memory. *Nature* 522, 309–314.
- Tang, W., and Jadhav, S.P. (2019). Sharp-wave ripples as a signature of hippocampal-prefrontal reactivation for memory during sleep and waking states. *Neurobiol. Learn. Mem.* 160, 11–20.
- Tang, W., Shin, J.D., Frank, L.M., and Jadhav, S.P. (2017). Hippocampal-Prefrontal Reactivation during Learning Is Stronger in Awake Compared with Sleep States. *J. Neurosci.* 37, 11789–11805.
- Todorova, R., and Zugaro, M. (2019). Isolated cortical computations during delta waves support memory consolidation. *Science* 366, 377–381.
- Tonegawa, S., Morrissey, M.D., and Kitamura, T. (2018). The role of engram cells in the systems consolidation of memory. *Nat. Rev. Neurosci.* 19, 485–498.
- Vaz, A.P., Inati, S.K., Brunel, N., and Zaghoul, K.A. (2019). Coupled ripple oscillations between the medial temporal lobe and neocortex retrieve human memory. *Science* 363, 975–978.
- Wilson, M.A., and McNaughton, B.L. (1994). Reactivation of hippocampal ensemble memories during sleep. *Science* 265, 676–679.
- Yagi, S., Igata, H., Shikano, Y., Aoki, Y., Sasaki, T., and Ikegaya, Y. (2018). Time-varying synchronous cell ensembles during consummatory periods correlate with variable numbers of place cell spikes. *Hippocampus* 28, 471–483.
- Yamamoto, J., and Tonegawa, S. (2017). Direct Medial Entorhinal Cortex Input to Hippocampal CA1 Is Crucial for Extended Quiet Awake Replay. *Neuron* 96, 217–227.e4.

STAR★METHODS

KEY RESOURCES TABLE

REAGENT or RESOURCE	SOURCE	IDENTIFIER
Chemicals		
CaCl ₂ ·2H ₂ O	Nacalai Tesque	cat. no. 06730-15
MgCl ₂ ·7H ₂ O	Nacalai Tesque	cat. no. 20908-65
MgSO ₄ ·7H ₂ O	Nacalai Tesque	cat. no. 21002-85
D-glucose	Nacalai Tesque	cat. no. 16806-25
K-gluconate	Sigma-Aldrich	cat. no. 299-27-4
KCl	Nacalai Tesque	cat. no. 7447-40-7
HEPES	Sigma-Aldrich	cat. no. H4034-500G
Mg-ATP	Sigma-Aldrich	cat. no. A9187-500MG
Na ₂ -GTP	Sigma-Aldrich	cat. no. G8877-25MG
Biocytin	Sigma-Aldrich	cat. No. B4261-5MG
Materials		
Thick-walled borosilicate glass tubing (outer diameter: 1.5 mm, inner diameter: 0.84 mm)	World Precision Instruments	cat. no. 1B150F-4
Patch pipette fillers with a solution filter	Patch pipette fillers with a solution filter	Patch pipette fillers with a solution filter
Equipment		
Patch-clamp amplifier	Molecular Devices	MultiClamp 700B
Multiunit recording system	Blackrock	Cereplex Direct
Horizontal electrode puller	Sutter Instruments	P-1000 horizontal puller
Syringe pressurizer (10 mL)	Terumo	N/A
Deposited data		
Behavior and spike data	Mendeley Data	https://dx.doi.org/10.17632/kc49ctr6yb.1
Experimental models: organisms/strains		
Sprague Dawley rat	Japan SLC	slc:SD
Software and algorithms		
MATLAB R2018b	MathWorks	https://www.mathworks.com/products/matlab.html?s_tid=hp_products_matlab
MClust	By A. David Redish	http://redishlab.neuroscience.umn.edu/MClust/MClust.html
CerePlex Direct Software Suite	Blackrock Microsystems	https://www.blackrockmicro.com/technical-support/software-downloads/
pCLAMP 10.1 software	Molecular Devices	https://www.moleculardevices.com/products/axon-patch-clamp-system/acquisition-and-analysis-software/pclamp-software-suite

RESOURCE AVAILABILITY

Lead contact

Further information and requests for resources and reagents should be directed to and will be fulfilled by the Lead Contact, Takuya Sasaki (tsasaki@mol.f.u-tokyo.ac.jp).

Materials availability

This study did not generate any unique reagents. The CAD files for creating the feeding wheel and feeding port by 3D printers are available from the lead contact upon request.

Data and code availability

The original data are provided on Mendeley Data (<https://dx.doi.org/10.17632/kc49ctr6yb.1>). The codes are available from the lead contact upon request.

EXPERIMENTAL MODEL AND SUBJECT DETAILS

All experiments were performed with approval of the experimental animal ethics committee at the University of Tokyo (approval number: A30-72) and according to the NIH guidelines for the care and use of rats.

All Sprague Dawley male rats (3–5 weeks old) were purchased from SLC (Shizuoka, Japan). The rats were housed individually and maintained on a 12-h light/12-h dark schedule with lights off at 7:00 AM.

All behavioral experiments occurred in the dark phase. Following at least 1 week of adaptation to the laboratory, the rats were housed individually and reduced to 85% of their *ad libitum* weight through limited daily feeding. Water was readily available.

In total, 16 rats were trained in the U track task and used for recordings of local field potential (LFP) signals from the hippocampus (HPC). On days with recordings, 8 rats performed only a familiar U track task, and 8 rats first performed a familiar U track task followed by a novel U track task. All rats were then head-fixed under awake conditions. In addition, to confirm the physiological and morphological characteristics of mPFC neurons, whole-cell recordings of mPFC neurons were obtained from 9 rats (Figure S2E). To confirm the animal's awake states, LFP recordings from the mPFC were obtained from 3 rats (Figures S1C and S1D).

METHOD DETAILS

Behavioral training on a U-shaped track

Before surgery, the rat was trained daily for at least 3 days to perform a U-shaped track task (Figure 1A). On one training day, the rat was trained to run back and forth on a U-shaped track consisting of three 70 × 9 cm² alleyways (with small sides rising 0.5 cm above the surface of the arm, 29 cm elevated from the floor) to obtain a constant amount of ~0.2 mL of chocolate milk reward placed at the track end during a 10–15-min session.

This training was repeated daily for 10 min until the rat consumed the reward at least 30 times within a 10-min training period. The rat was maintained on a pedestal with a diameter of 20 cm outside the track for 10 min before and after the task. After achieving the aim in the training phase, surgery was performed.

Surgical procedures

Pictures of the experimental instruments used for surgery are shown in Figure S1A. A standard electrode assembly for multiunit recording, called a microdrive, was prepared as described previously (Jog et al., 2002; Kloosterman et al., 2009; Nguyen et al., 2009). The rat was anesthetized with isoflurane gas (2%–2.5%) and then fixed in a stereotaxic instrument with two ear bars and a nose clamp. An incision was made from the area between the eyes to the back of the head. A rectangular craniotomy with a size of 1.2 × 2 mm was performed above the right hippocampus (3.6 mm posterior and 3.0–5.0 mm lateral to bregma) using a high-speed drill, and the dura was surgically removed. Two stainless-steel screws were implanted in the bone above the cerebellum to serve as ground and reference electrodes. A microdrive that consisted of 8 independently movable tetrodes, which was created using a 3D printer (Form 2, Formlabs) (Aoki et al., 2019; Okada et al., 2017; Yagi et al., 2018), was stereotaxically implanted (Figure S1A). The tip of the electrode bundle was lowered to the cortical surface, and the electrodes were inserted 0.75 mm into the brain at the end of surgery. The electrodes were constructed from 17- μ m-wide polyimide-coated platinum-iridium (90/10%) wire (California Fine Wire), and the electrode tips were plated with platinum to lower electrode impedances to 180–300 k Ω at 1 kHz. The microdrive was physically protected by a cone-shaped plastic cover (13 mm height, 13 mm diameter in the top circle, 30 mm diameter in the bottom circle). To reduce its weight, the plastic cover had 36 elliptical holes 4 mm in the major axis and 2 mm in the minor axis.

In addition to microdrive implantation, a craniotomy with a diameter of ~1.3 mm was performed above the mPFC (2.5–3.5 mm anterior and 1.0–1.5 mm lateral to bregma). The dura was not removed during this procedure. To physically protect the craniotomy, polyimide tubing (3.5 mm height, 1.42 mm diameter) was vertically implanted on the craniotomy above the dura (Figure S1A). In addition, a quadrant-shaped plastic cover (~20 mm size, 5 mm height), which was created using a 3D printer, was placed on the skull surrounding the craniotomy, which protected the craniotomy from dental cement invasion and served as a pool for placing a ground electrode during subsequent patch-clamp recordings.

Finally, all of the wires, the Microdrive, and the cover were secured to the skull using stainless-steel screws and dental cement. Following surgery, the rat was housed individually in a transparent Plexiglass cage with free access to water and food for at least 3 days. After recovery from surgery, food was restricted to 85% according to their body weight.

Adjusting electrode depth

After the surgery, the rat was connected to the recording equipment via Cereplex M (Blackrock), a digitally programmable amplifier, close to the rat's head. The output of the headstage was conducted via a lightweight multiwire tether to the Cereplex Direct recording system (Blackrock). Electrode turning was performed while the rat rested on the pedestal. The electrode tips were advanced slowly 25–250 μm per day for 10–17 days until spiking cells were encountered in the CA1 or CA2 layer of the hippocampus, which was identified on the basis of LFP signals and single-unit spike patterns. Once the tetrodes were adjacent to the cell layer, as indicated by the presence of low-amplitude multiunit activity, tetrodes were settled into the cell layer for stable recordings over a period of several days.

During the several days of this turning period, the rat was again trained, similar to the presurgery trainings. This postsurgery training lasted for at least 10–17 days before performing electrophysiological recording. Postsurgery training was performed with the recording headstage and cable attached to the rat's head so that the rat became familiar with the recording conditions.

In addition, during this turning period, the rat was trained to habituate to head fixation for subsequent patch-clamp recordings, as described previously (Lee and Lee, 2017). The rat's head was stereotaxically fixed using a plastic headplate and left undisturbed for ~ 10 min on the first day (Figure S1B). A chocolate milk drop was sometimes provided to the fixed rat. The time of habituation was gradually increased to 30 min over the course of 10–17 days. This habituation training commenced until the rat sat quietly for several minutes without movement.

Electrophysiological recording in U track tasks

Electrophysiological data recordings during the U track task began after the rats again achieved the aim as in the postsurgery training phase, and stable well-separated unit activity was identified in the hippocampus. On a recording day, the rat was first maintained on the pedestal outside the track for 10 min, termed a pre-rest session, before and after the task. The rat then performed the U track task for 10–15 min. As the behavioral paradigm was completely identical to that of the training phases, this session was termed a familiar U track session. In some cases, the U track was rotated counterclockwise by 90 degrees without changing any external cues. As this positioning of the track was novel to the rats, this session was termed a novel U track session.

LFP recordings were sampled at 2 kHz and filtered between 0.1 and 500 Hz. Unit activity was amplified and bandpass filtered at 600 Hz to 6 kHz. Spike waveforms above a trigger threshold (60 μV) were time-stamped and recorded at 30 kHz for 1.6 ms. To monitor the rat's moment-to-moment position, a near-infrared reflection sticker was attached to the microdrive on the animal's head, and the position of the sticker was tracked at 25 Hz using an infrared camera (MCM-303NIR, Gazo, Japan) attached to the ceiling, which was sampled by a laptop computer.

In vivo patch-clamp recordings

After the U track tasks, the rat was fixed to the stereotaxic apparatus, as in the training habituation. Lidocaine solution (0.05 mg/kg, ~ 1 ml) was applied to the pool surrounded by the plastic cover above the mPFC craniotomy as an analgesic. The polyimide tubing was then removed from the skull. For inserting a patch pipette, a hole with a diameter of ~ 1 mm in the dura was gently opened using a 30-gauge stainless needle. Through the hole, a borosilicate glass pipette (4.0–7.0 M Ω), tilted at an angle of 10–15° to the posterior side, was lowered slowly to the mPFC, including the prelimbic or infralimbic cortex, at a depth of 750–3600 μm from the cortical surface (Figure S1B). Whole-cell recordings were obtained from neurons in these areas. The intrapipette solution consisted of the following reagents: 135 mM K-gluconate, 4 mM KCl, 10 mM HEPES, 10 mM, Na₂-phosphocreatine, 4 mM Mg-ATP, 0.3 mM Na₃-GTP, 0.3 mM EGTA, and 0.2% biocytin. The solution was adjusted to pH 7.3 and 285–289 mOsm. The signal was amplified with a MultiClamp 700B, analyzed with pCLAMP10.1 (Molecular Devices, Union City, CA) and digitized at 20 kHz. At the beginning of each experiment, depolarizing and hyperpolarizing 1000-ms rectangular currents from -200 to $+350$ pA were injected into the cell at steps of 50 pA to characterize the cell's intrinsic properties and spike responses. In the whole-cell current-clamp configuration, current steps (1000 ms) were applied; only cells that showed typical regular-spiking characteristics of principal cells were selected (Figure S2E). The liquid junction potential was nulled offline. Cells were discarded when the series resistance exceeded 75 M Ω or the mean resting potential exceeded -50 mV. Moreover, recordings were truncated when the spike peak decreased below -10 mV or the resting potential increased by more than 40 mV from its value at the onset of the recording. Throughout this recording process, no signs of painful behavior were observed. Under awake conditions, one and two cells were recorded from 14 and 2 rats, respectively.

Histological analysis to confirm tetrode locations and patch-clamped cells

After patch-clamp recordings, the rat received an overdose of urethane and was perfused intracardially with 4% paraformaldehyde in phosphate-buffered saline (PBS) (pH 7.4) and decapitated. To aid the reconstruction of electrode tracks, the electrodes were not withdrawn from the brain until 12 hours after perfusion. After dissection, the brain was fixed overnight in 4% PFA and then coronally cut into two tissues, one containing the prefrontal cortex and the other containing the hippocampus. The tissue containing the prefrontal cortex was sliced coronally at a thickness of 100–150 μm in PBS using a vibratome (Dosaka). The slices were incubated with 2 $\mu\text{g/ml}$ streptavidin-Alexa Fluor 594 conjugate and 0.2% Triton X-100 for 6 hours, followed by incubation with 0.4% NeuroTrace 435/455 blue fluorescent Nissl Stain (Thermo Fisher Scientific; N21479) overnight. The slices were analyzed with an FV1200 (Olympus, Tokyo, Japan) confocal system under 20 \times and 40 \times objectives. Z series images were collected with 1.14- μm steps, and 4 Z sections (1 μm thick) were stacked using ImageJ (NIH). The other tissue containing the hippocampus was equilibrated with a sequence of 20%

sucrose and 30% sucrose in PBS. Frozen coronal sections (100–150 μm) were cut using a microtome, and serial sections were mounted and processed for cresyl violet staining. For cresyl violet staining, the slices were rinsed in water, counterstained with cresyl violet, and coverslipped with mounting agent (PARAmount-D, Falma). The positions of all tetrodes in the CA1 or CA2 regions were confirmed by identifying the corresponding electrode tracks in histological tissue. Recordings were included in the data analysis if the tetrode's deepest position was in the cell layer.

QUANTIFICATION AND STATISTICAL ANALYSIS

Spike sorting of hippocampal neurons

Spike sorting was performed offline using the graphical cluster-cutting software MClust (Redish, 2009). Sleep recordings before and after the behavioral paradigms were included in the analysis to assure recording stability throughout the experiment and to identify hippocampal cells that were silent during behavior. Clustering was performed manually in 2D projections of the multidimensional parameter space (i.e., comparisons between waveform amplitudes, the peak-to-trough amplitude differences, and waveform energies, each measured on the four channels of each tetrode) (Figure S2C). Cluster quality was measured by computing the L_{ratio} and the isolation distance (Schmitzer-Torbert et al., 2005). The L_{ratio} was computed by the original equation, proposed by Schmitzer-Torbert et al. (2005), not normalized by the total number of spikes recorded on the tetrode. A cluster was considered as a cell when the L_{ratio} was less than 0.30 and the isolation distance was more than 15 (Figure S2D; average L_{ratio} was 0.113 ± 0.007 and average isolation distance was 34.7 ± 2.9 in 135 isolated cells). In the auto-correlation histograms, cells with no clear refractory period (< 3 ms) were excluded from analyses (Csicsvari et al., 1999; Harris et al., 2000). In addition, in the cross-correlation histograms, putative cell pairs with a symmetrical gap around the center bins were considered to arise from the same cell and were merged. Finally, cells with spike waveforms longer than 300 μs and an average firing rate of less than 3 Hz throughout an entire recording period were considered putative excitatory cells and included in the analysis.

Spatial firing patterns of individual hippocampal neurons

For analyzing spike patterns, the animal's coordinates and the positions of spikes of individual cells were projected onto a centerline of alleyways corresponding to each trajectory. The average firing-rate distribution on each trajectory ("R1 to R2" or "R2 to R1") was separately computed along the projected line by dividing the total number of spikes in each location bin (10 cm) by the total time that the rat spent in that bin. The location bins of the reward area were excluded from subsequent analyses as the duration the rat spent in these areas was considerably different from those elsewhere on the track. All firing-rate distributions were smoothed by a one-dimensional convolution with a Gaussian kernel with a standard deviation of one pixel (10 cm). A place cell in a task was defined as a cell based on the two following criteria: (1) the average firing-rate distribution on a trajectory in a session had a maximum firing rate of more than 1 Hz (i.e., the absolute maximum firing rate), and (2) the maximum firing rate exceeded 2 standard deviations (SDs) above the mean, where the SD and the mean were computed from the series of firing rates except the maximum firing rate in that distribution. For each place cell, a place field center was defined as the position giving the maximum firing rate in the distribution. Under this criterion, some place cells had one place field in either one of two trajectories, whereas the others had two place fields in both trajectories. The other cells that did not meet the criteria were classified as non-place cells. For a given place cell pair, the distance between the two place field centers was computed, termed the place field distance. Place cell pairs with place field distances less than 30 cm and more than 60 cm were classified as close and distant place cell pairs, respectively.

For each place cell identified in the novel task, spatial firing patterns were compared between the familiar and the novel task (Figure S2I). Place fields that shifted their field center with a distance of 20 cm or less and 30 cm or more across the two tasks were classified as "stable" and "remap," respectively. Place fields that newly emerged in the novel task were classified as "appear."

Detection of HPC synchronized spikes and SWRs

During patch-clamp recordings, synchronization events of HPC neuronal spikes were detected when two or more HPC neurons were simultaneously activated in a time window of 100 ms. The onset of HPC synchronization events was defined at the time point when the first spike was observed. To detect SWRs from HPC LFP signals, the electrode including the largest number of HPC pyramidal cells identified in the spike sorting process was used. The HPC LFP signal was bandpass filtered at 150–250 Hz, and the root mean-square power was calculated in the ripple band with a bin size of 20 ms. The threshold for SWR detection was set to 3 standard deviations (SDs) above the mean (Carr et al., 2011), unless otherwise specified. In Figure S4A, the threshold was set to 3–6 SDs above the mean. The onset of SWRs was marked at the point when the ripple power first exceeded 2 SDs above the mean.

Detection of neocortical oscillations

To detect slow waves, mPFC LFP signal was bandpass filtered at 1–10 Hz, and the root mean-square power was calculated with a bin size of 1 s. The power during an active wakefulness of 2 min was considered as a baseline power, and a slow wave was detected when the power exceeded 1.5 times of the baseline (Narikiyo et al., 2020). To detect delta oscillations, mPFC LFP signal was bandpass filtered at 2–6 Hz, and the root mean-square power was calculated with a bin size of 100 ms. A delta oscillation was detected when the power exceeded 2 standard deviations (SDs) above the mean of the power for 150–500 ms (Todorova and Zugaro, 2019). To detect spindle oscillations, mPFC LFP signal was bandpass filtered at 7–10 Hz, and the root mean-square power was calculated

with a bin size of 20 ms. The threshold for spindle oscillation detection was set to 3.5 standard deviations (SDs) above the mean (Latchoumane et al., 2017). During awake head-fixed periods in the conditions of our patch-clamp recordings, no oscillations were detected as shown in Figures S1C and S1D.

Membrane potential changes in mPFC neurons during HPC synchronization

From mPFC patch-clamp recording data, membrane potential changes in the mPFC at the time of HPC synchronization or SWR events were computed. For all the following analyses, only HPC events that were temporally separated by more than 200 ms from prior SWR events were analyzed. This procedure excluded the second and subsequent events that were possibly involved in ripple bursts (Yamamoto and Tonegawa, 2017). For each HPC event, a difference in average mPFC membrane potentials between 0–150 ms after and 50–200 ms before the HPC event was computed, termed mPFC ΔV_m , unless otherwise specified. In Figure S4, mPFC ΔV_m was computed as a difference in mPFC V_m between 0–150 ms and 200–350 ms before HPC events (Figure S4F) and between 350–500 ms after and 50–200 ms before HPC events (Figure S4G). To assess whether a distribution of mPFC ΔV_m was observed above chance level, a surrogate distribution was constructed with the same procedure from 1000 surrogate datasets in which the same mPFC ΔV_m was extracted at random time points in the same dataset. The original distribution was considered to be significant when there was a significant difference between the original and surrogate distribution computed by the Kolmogorov-Smirnov test. In Figures S4D and S4E, the same analysis was applied to HPC SWRs instead of HPC synchronization. Here, 17 mPFC cells from 15 rats with more than 10 HPC SWRs were analyzed.

Prediction of mPFC membrane potential changes from HPC synchronized spike patterns

Using linear regression analysis, we predicted the mPFC ΔV_m of a place cell during a patch-clamp period from synchronized spike patterns of HPC neuronal ensembles (Figures 2D–2G). Data with more than 4 HPC cells were analyzed ($n = 13$ mPFC cells from 13 rats). A predictor vector s was defined as spike patterns of all HPC cells in individual HPC synchronization events with at least 3 spiking HPC cells, and a target variable v was set as the corresponding mPFC ΔV_m of a whole-cell recorded mPFC cell. For each HPC synchronization event, a vector of weighted coefficients w was computed so that the weighted linear sum $v' (= s \cdot w)$ was fitted against v . In each HPC synchronization event, a leave-one-out cross-validation analysis was applied to examine the predictability of the target variable.

For more detail, for the l -th HPC synchronization event, a $(N+1)$ -dimensional predictor vector was defined as a population vector s_l , the N -dimensional entries of which were the binary indexes representing the presence or absence of spikes (1 for one or more spikes, 0 for no spike) of individual HPC cells during the l -th HPC synchronization event, where N denotes the total numbers of HPC cells, and the $(N+1)$ -th entry was set at +1 as a constant term. For a whole-cell recorded mPFC neuron, a target variable v_l was set as the mPFC ΔV_m during the l -th HPC synchronization event. A linear regression function was applied to estimate a linear relationship between a series of predictor vectors, $S = (s_1, s_2, s_3, \dots, s_L)^T$, and a series of target variables, $v = (v_1, v_2, v_3, \dots, v_L)^T$, where L denotes the total number of HPC synchronization events and is greater than $(N+1)$. The best $(N+1)$ -dimensional weighted vector w was mathematically computed as follows:

$$w = S^+ v,$$

where

$$S^+ = (S^T S)^{-1} S^T.$$

To evaluate the predictability of the l -th target variable v_l , leave-one-out cross-validation was performed by computing w from the dataset without s_l and v_l . A predicted target variable v'_l was calculated as follows:

$$v'_l = s_l^T w.$$

The same analyses were repeated for all L HPC synchronization events, and a series of predicted variables v' were compared with the observed variables v , as shown in Figure 2D. The accuracy of the prediction during the timescale of an entire recording session was assessed by computing a prediction error as an average absolute difference between the two variables, v and v' . To evaluate the significance of a prediction error in real data, errors were computed with the same procedures from 1000 surrogate datasets created by shuffling the order of observed variables v across all HPC synchronization events (Figure 2D, bottom). A z-score of a prediction error was computed based on a distribution of 1000 prediction errors from 1000 surrogate datasets, and a prediction score for an mPFC neuron was defined as the negative value of the z-score. A prediction score of 1.96 was set as a threshold to define cells with significantly positive prediction scores ($p < 0.05$) as this z-score represents the approximate value suggesting 95% confidence intervals in the normal distribution of surrogate datasets.

Statistics

All data are presented as the mean \pm standard error of the mean (SEM) and were analyzed using MATLAB. Comparisons between real and surrogate distributions were analyzed by the Kolmogorov-Smirnov test in Figure 2. Comparisons between two datasets were analyzed by the Mann-Whitney U test in Figures 3 and 4. Multiple group comparisons were performed by Mann-Whitney U test followed by post hoc Bonferroni corrections after Kruskal-Wallis test. The null hypothesis was rejected at the $p < 0.05$ level.

Cell Reports, Volume 34

Supplemental information

**Prefrontal synaptic activation
during hippocampal memory reactivation**

Yuya Nishimura, Yuji Ikegaya, and Takuya Sasaki

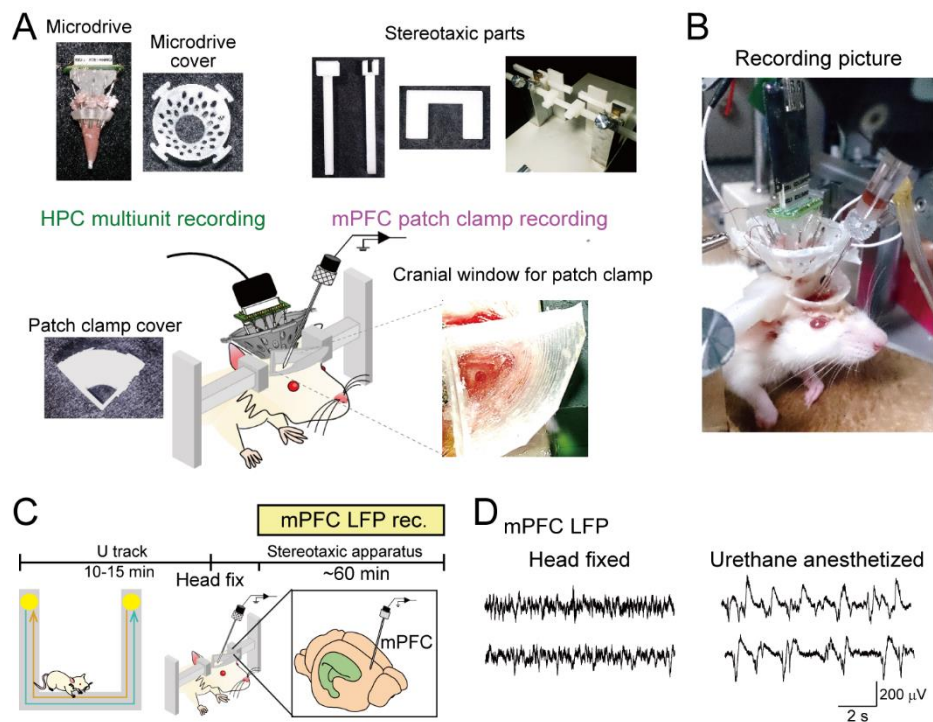
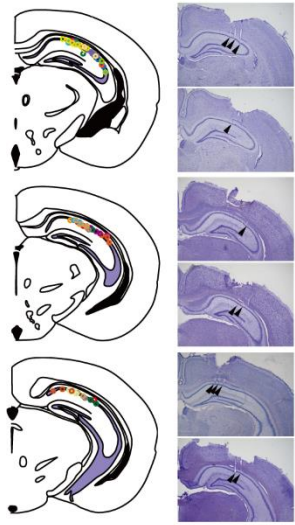


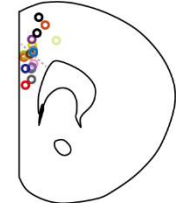
Figure S1. Pictures of the experimental materials used for the recording system.

Related to Figure 1. (A) The bottom drawing shows a schematic illustration of simultaneous multiunit tetrode recordings from hippocampal neurons and a whole-cell recording from a mPFC neuron from a head-fixed awake rat. On the day of surgery, the rats were implanted with 8 tetrodes directed at the HPC, and a craniotomy was created over the mPFC for patch-clamp recordings. The tetrodes were lowered for 10–17 days until spiking cells were encountered in the pyramidal cell layer of the hippocampus. (Left top) A microdrive accommodating 8 tetrodes was used for HPC multiunit recordings. (Right top) A stereotaxic apparatus was fixed to the animal's head for mPFC patch-clamp recordings. On postsurgery training days, the rats were habituated to the head restraint apparatus. (Left bottom) A cover was used for protecting the cranial window for mPFC patch-clamp recordings. (Right bottom) A cranial window was made above the mPFC for mPFC patch-clamp recording. All custom-made plastic parts were created by a 3D printer. (B) An example showing simultaneous HPC multiunit recordings with the microdrive (back side) and an mPFC patch-clamp recording with a glass pipette (front side) in a head-fixed rat. (C) To estimate animal arousal states in the conditions of mPFC patch-clamp recordings in our study, we tested whether the awake head-fixed condition induced delta and spindle oscillations in the mPFC. Rats were head-fixed on a stereotaxic apparatus, and mPFC signals were recorded after the rats performed a U track task, with the same procedures as in the main figures. (D) No apparent slow, delta, or spindle oscillations were observed from mPFC LFP signals from the head-fixed rats ($n = 3$ rats), whereas typical slow oscillations emerged in the mPFC under urethane-anesthetized conditions.

A Hippocampus multiunit recording

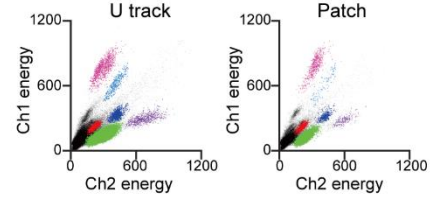


B PFC patch-clamp recording

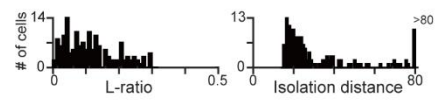


- Rat # 59
 - Rat # 62
 - Rat # 66
 - Rat # 69
 - Rat # 71 (x2)
 - Rat # 79
 - Rat # 80 (x2)
 - Rat # 82
 - Rat # 140
 - Rat # 141
 - Rat # 149
 - Rat # 151
 - Rat # 162
 - Rat # 168
 - Rat # 170
 - Rat # 171
- HPC LFP only

C Rat162 HPC TT2



D All HPC cells used for analysis



E

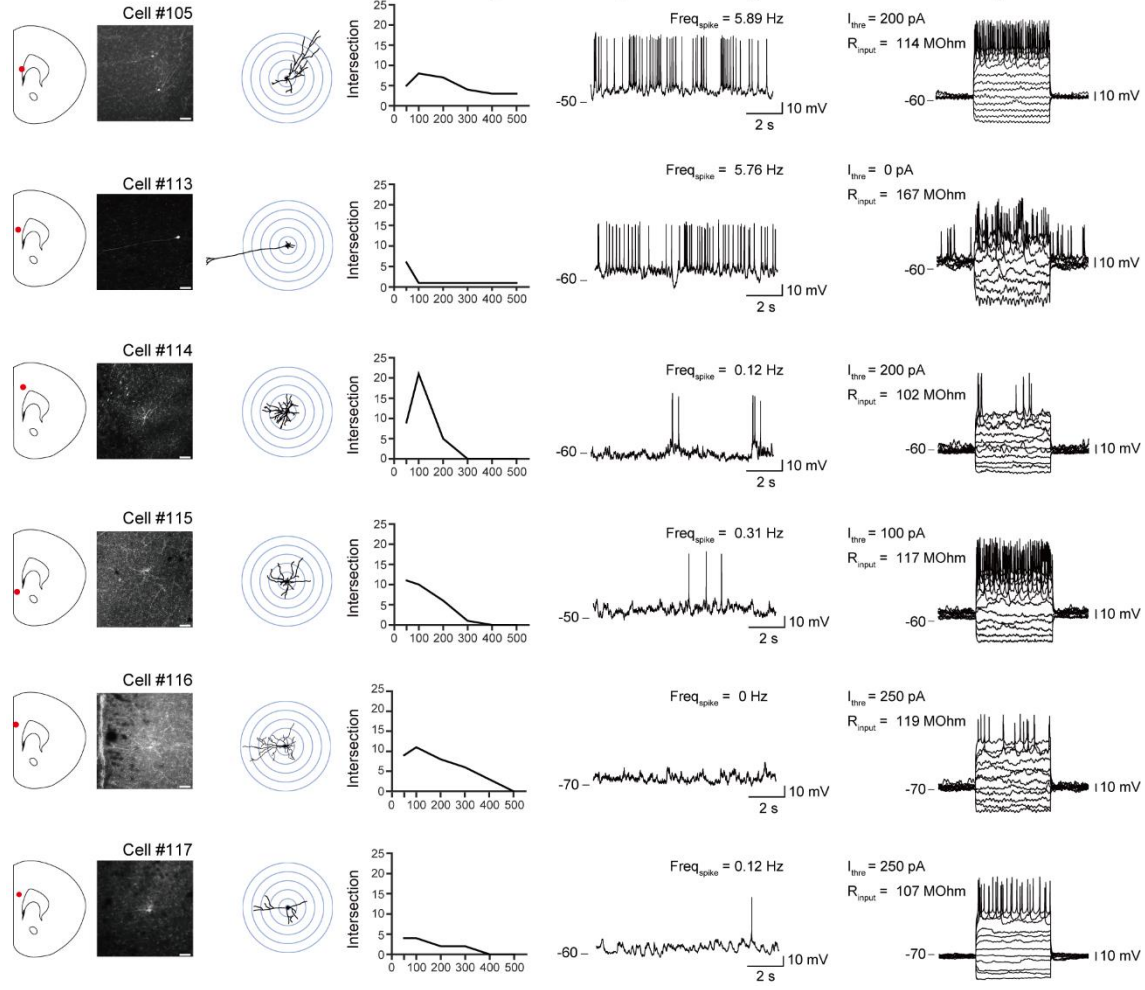


Figure S2. Confirmation of recordings. Related to Figure 1. (A) (Left) Superimpositions of recording sites for all 83 tetrodes (from 16 rats) on the dorsal HPC cell layer in sequential coronal brain sections. Each circle represents each tetrode. (Right) Typical pictures of cresyl-stained sections, with the arrowheads indicating the tips of tetrode tracks. (B) Recording sites for 18 whole-cell recordings in the mPFC that were performed with HPC multiunit recordings in awake rats ($n = 16$ rats). The gray dotted line represents the border to define the prelimbic (PL) region and the anterior cingulate cortex (ACC) for analyses in Supplementary Fig. 4N and 4O. The morphology of typical whole-cell recorded neurons is shown in E. In some rats, mPFC neuronal morphology was not precisely reconstructed due to accidental disruption of the patch. Recording sites in these rats were estimated based on the XYZ coordinates of electrodes manipulated above the skull. (C) Projection patterns of the energy of multiunit signals recorded from two channels in a representative single tetrode. Each panel shows a recording phase (U track task and Patch-clamp recording) for the same channel. Each dot represents one spike, and each color represents a cluster that was assigned to a single cell. The patterns of these spike clusters remained stable over the recording periods. (D) Distributions of L_{ratio} and isolation distance for individual HPC neuronal units ($n = 135$ neurons from 13 rats used for main analyses) identified by multiunit spike sorting. (E) Characteristics of mPFC neurons recorded by whole-cell recordings. Each row represents a cell. From left to right, a recording site in the mPFC (red dot), a fluorescent image of a mPFC neuron labeled with biocytin, a reconstructed neuron morphology with the circles depicted with diameters that increased in 100- μm intervals starting from 50 μm , a result of the Sholl analysis applied to the reconstructed morphology, a 10-s ongoing membrane potential trace, and membrane potential traces in response to step current injection (from -200 pA to $+350$ pA, 1000 ms, shown as the bottom panel).

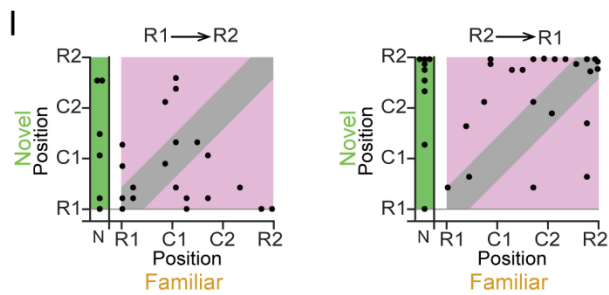
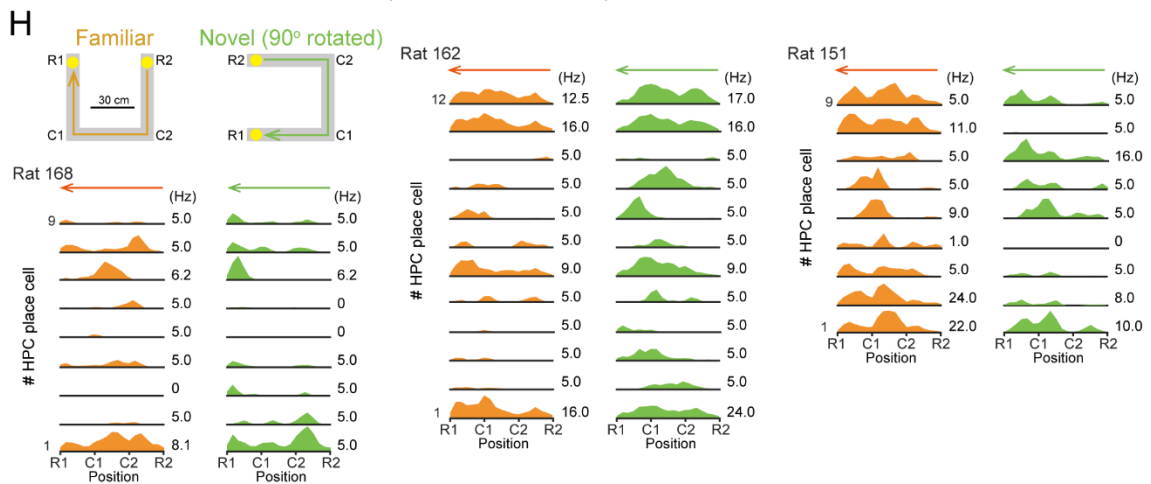
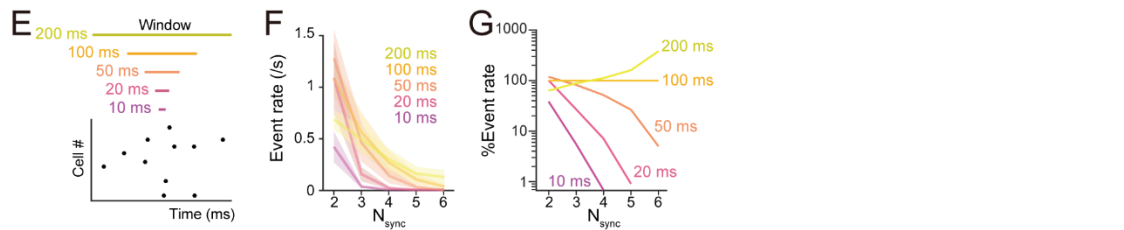
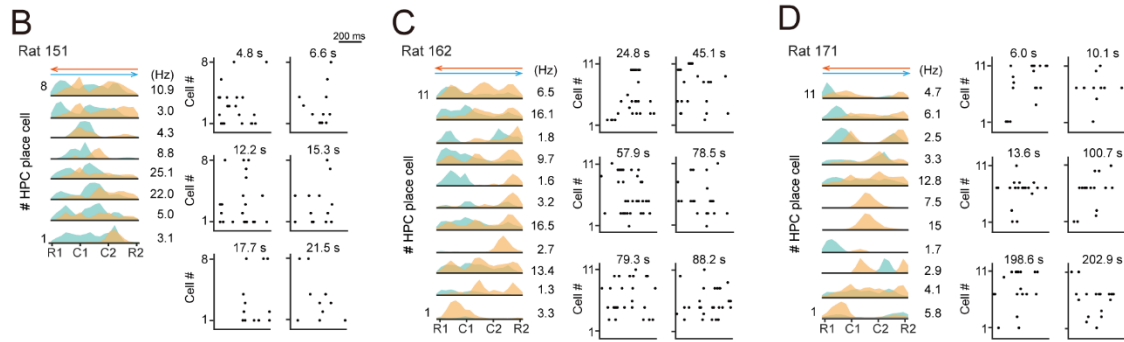
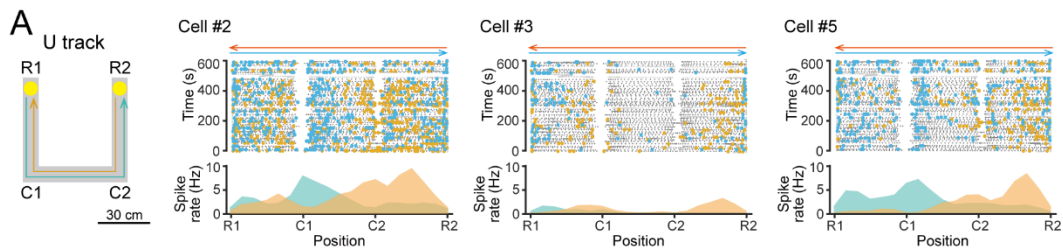


Figure S3. Reactivation of HPC place cells during mPFC patch-clamp recordings.

Related to Figure 1 and 4. (A) Spatial firing patterns of three representative HPC pyramidal cells recorded during the U track task. (Top) Animal positions linearized on the U track are shown by gray dots, which are superimposed by colored dots showing spike positions. Spike locations were separately plotted for each trajectory pattern (orange and cyan). (Bottom) Averaged firing-rate distributions over all trials plotted as a function of position. (B-D) In each panel, the left column shows the averaged firing-rate distributions of HPC place cells as a function of positions linearized on the U track. The maximum firing rates on the Y-axis are listed as values (in Hz). Right panels show representative raster plots of synchronized spikes observed from these cell populations during mPFC whole-cell recordings. The limited number of place cell spikes that occurred during the patch-clamp recordings precluded the analysis of place cell replay patterns. (E) Schematic illustration of computing the number of HPC cells in each synchronization event from a raster plot with different time windows (10, 20, 50, 100, and 200 ms) labeled in different colors. (F) The rates of HPC synchronization events plotted against the number of synchronized HPC neurons (N_{sync}) ($n = 13$ rats used for mPFC patch-clamp recordings). Thick lines and thin regions show the averages and SEM, respectively. Each color represents each time window, as shown in E. (G) The averages at individual time windows shown in F were normalized by those at a time window of 100 ms (used in the main analyses). (H) HPC place cells in the novel U track task. For three representative rats, the spatial firing distributions of HPC cells were compared between the familiar and novel U track tasks. The maximum firing rates on the Y-axis are listed as values (in Hz). (I) Classification of place fields of place cells (novel). For each place cell (novel), the position of the place field center in the novel task was plotted against that in the familiar task ($n = 28$ fields from R1 to R2 and $n = 32$ fields from R1 to R2 from 42 place cells (novel)). Each dot represents each cell. Areas under R1, indicated by N, represent cells that exhibited no spatial firing in the familiar task. Different types of changes in spatial firing patterns are shown in different colored areas as follows: green, appear; light magenta, remap; gray, stable in the novel task.

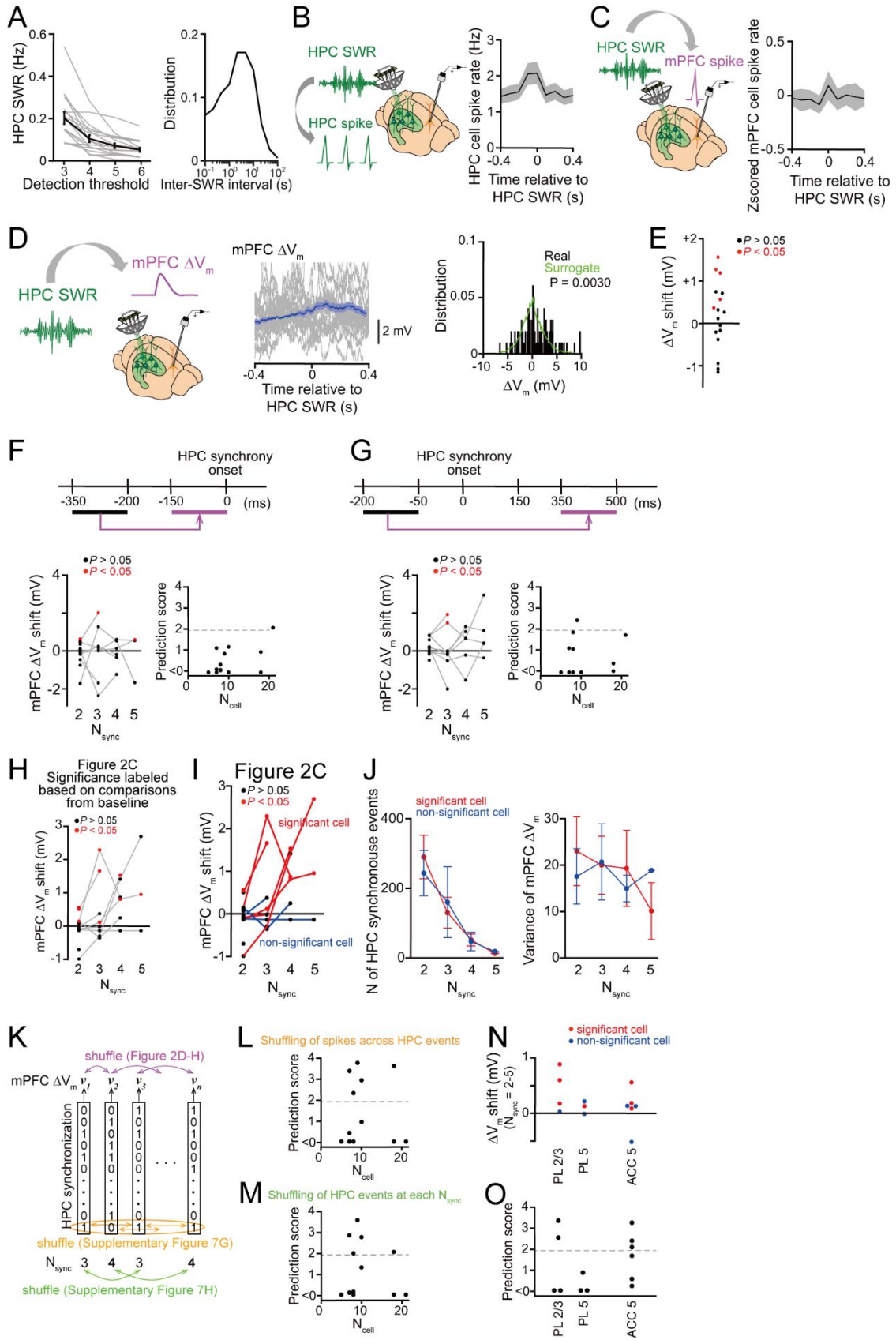


Figure S4. Relationship between HPC SWRs and spike patterns during mPFC patch-clamp recordings. Related to Figure 2. (A) (Left) The frequencies of HPC SWRs during mPFC whole-cell recordings at different detection thresholds from 3 to 6 standard deviations (SDs) above the mean in the root-mean-square power trace. Each gray line represents a recording, and the black line represents their average and SEM ($n = 16$ rats). A threshold of 3 SDs above the mean was selected in all analyses. (Right) Distribution of inter-SWR intervals detected at a threshold of 3 SDs above the mean ($n = 15$ rats with HPC SWRs). (B) HPC SWR-triggered spike rate changes in HPC neurons ($n = 114$ cells from 12 rats with HPC SWRs) in awake rats during mPFC whole-cell recordings with a duration of 335 ± 63 s. Within these limited recording periods, SWR-triggered spike rate increases in HPC neurons could be detected. (C) HPC SWR-triggered spike rate changes in mPFC neurons ($n = 17$ cells from 15 rats with HPC SWRs) in awake rats during mPFC whole-cell recordings. Similar to previous observations, HPC SWR-associated spike rate increases in mPFC neurons could be detected in our recording periods. (D) Changes in membrane potentials of an mPFC cell during the emergence of HPC SWRs. (Left) Representative mPFC ΔV_m traces aligned to the onset of HPC SWRs in an awake rat. Each gray line represents a trace corresponding to each HPC SWR, and the blue thick line and blue thin region represent their average and SEM, respectively. (Right) Distribution of the mPFC ΔV_m at the time of HPC SWRs, constructed from the left traces. The green line shows a distribution computed from 1000 surrogate datasets in which the time of HPC SWR events was randomly shuffled. (E) Average distribution shifts in mPFC membrane potential changes in HPC SWRs. Each dot represents a mPFC cell ($n = 17$ cells from 15 rats with HPC SWRs). For each mPFC cell, a P -value was computed by a comparison between real and surrogate distributions by Kolmogorov-Smirnov test. Red dots show statistically significant results. (F, G) Supplementary analyses for the relationship between HPC synchronization events and mPFC ΔV_m in Fig. 2C and Fig. 2G. No apparent relationships between HPC synchronization events and mPFC membrane potential changes in reversed and remote time windows were observed compared with the time window used in Fig. 2. The same analyses as in Fig. 2C and 2G were performed with two different time windows, a pre-event 0–150-ms window (F) and a post-event 350–500-ms window (G). The left panels were created as in Fig. 2C and show the average shifts in the mPFC ΔV_m distribution plotted against the number of synchronized HPC neurons ($n = 13$ mPFC cells from 13 rats with >4 HPC cells). Each line represents a recording. For each plot, a P -value was computed by a comparison between real and surrogate distributions by Kolmogorov-Smirnov test. Red dots show statistically significant results. Compared with Fig. 2C with a post-event 0–150-ms window, a smaller fraction of neurons showed significant data points. The right panels were created as in Fig. 2G and show prediction scores of all 13 rats plotted against the number of HPC neurons. Significantly predicted fractions with $P < 0.05$ defined by prediction scores are shown above the gray horizontal dotted lines. Compared with Fig.

2G with a post-SWR 0–150-ms window, few significant prediction scores >1.96 were observed. (H) The same plots as Fig. 2C but a statistical test (Kolmogorov-Smirnov test) for each plot was performed between the distributions of mPFC ΔV_m in a post-event 0–150-ms window and those of the baseline mPFC ΔV_m . Red dots show statistically significant results. The significant effects were observed in 38.5%, 37.5%, 33.3%, and 33.3% of datasets at N_{sync} of 2, 3, 4, and 5, respectively. (I) The datasets shown in Fig. 2C were separately analyzed for significant cells that had at least one significant plots ($n = 7$ mPFC cells, shown in red lines) and non-significant cells that had no significant plots ($n = 6$ mPFC cells, shown in blue lines) at N_{sync} of 2–5. (J) (Left) The numbers of HPC synchronous events (used to compute for Fig. 2C) plotted against each N_{sync} of HPC cells. At N_{sync} of 2 to 4, no significant differences were found between significant and non-significant cells. $P > 0.05$, Tukey's test. Data at a N_{sync} of 5 were not analyzed due to limited sample size. (Right). The variance of mPFC ΔV_m distribution (used to compute for Fig. 2C) plotted against each N_{sync} of HPC cells. At N_{sync} of 2 to 4, no significant differences were found between significant and non-significant cells. $P > 0.05$, Tukey's test. (K) Schematic illustration of creating surrogate datasets for the prediction of mPFC membrane potential changes (v) from HPC synchronized spike patterns (s). In Fig. 2D–2H, surrogate datasets were created by shuffling the order of variables v across all HPC synchronization events (magenta). In Supplementary Fig. 4L, surrogate datasets were created by shuffling the order of HPC spikes across synchronization events with maintaining the total number of spikes in each cell (orange). In Supplementary Fig. 4M, surrogate datasets were created by shuffling the order of HPC synchronization events with the same N_{sync} to maintain the total numbers of HPC events for individual N_{sync} (green). (L, M) The same analyses as in Fig. 2G were performed with two different surrogate datasets as described in F. In both datasets, the patterns of mPFC neurons showing the significant effects were similar to those observed in Fig. 2G. (N) Shifts in average mPFC ΔV_m during all HPC synchronization events, as shown in Fig. 2C, were separately plotted for the different subregions (PL and ACC) and layers (layer 2/3 and layer 5) ($n = 13$ mPFC neurons from 13 rats with >4 HPC cells). Each dot represents each mPFC neuron. The cells were classified as significant cells (red, $n = 7$ cells) and non-significant cells (blue, $n = 6$ cells), as in I. (O) Prediction scores, as shown in Fig. 2G, were separately plotted for different subregions and layers ($n = 13$ mPFC neurons from 13 rats with >4 HPC cells). Each dot represents each mPFC neuron.